NAVAL POSTGRADUATE SCHOOL

Monterey, California

THESIS

THEORY FOR THE CEBAF AND SHIPBOARD FELS

by

Carl A. Bice

December, 1991

Thesis Advisor: William B. Colson

Approved for public release; distribution is unlimited

T257703

SECURITY CLASSIFICATION OF THIS PAGE

REPORT DOCUMENTATION PAGE

1a REPORT SECURITY CLASSIFICATION UNCALSS	1b RESTRICTIVE MARKINGS
2a SECURITY CLASSIFICATION AUTHORITY	3 DISTRIBUTION/AVAILABILITY OF REPORT Approved for public release; distribution is unlimited.
2b DECLASSIFICATION/DOWNGRADING SCHEDULE	
4 PERFORMING ORGANIZATION REPORT NUMBER(S)	5 MONITORING ORGANIZATION REPORT NUMBER(S)
6a NAME OF PERFORMING ORGANIZATION Naval Postgraduate School 6b OFFICE SYMBOL *(If applicable)* Code 61	7a NAME OF MONITORING ORGANIZATION Naval Postgraduate School
6c ADDRESS (*City, State, and ZIP Code*) Monterey, CA 93943-5000	7b ADDRESS (*City, State, and ZIP Code*) Monterey, CA 93943-5000
8a NAME OF FUNDING/SPONSORING ORGANIZATION 8b OFFICE SYMBOL *(If applicable)*	9 PROCUREMENT INSTRUMENT IDENTIFICATION NUMBER
8c ADDRESS (*City, State, and ZIP Code*)	10 SOURCE OF FUNDING NUMBERS Program Element No / Project No / Task No / Work Unit Accession Number
11 TITLE (*Include Security Classification*) THEORY FOR THE CEBAF AND SHIPBOARD FELS	
12 PERSONAL AUTHOR(S) Bice, Carl A.	
13a TYPE OF REPORT Master's Thesis 13b TIME COVERED From To	14 DATE OF REPORT (*year, month, day*) December, 1991 15 PAGE COUNT 81
16 SUPPLEMENTARY NOTATION The views expressed in this thesis are those of the author and do not reflect the official policy or position of the Department of Defense or the U.S. Government.	
17 COSATI CODES FIELD / GROUP / SUBGROUP	18 SUBJECT TERMS (*continue on reverse if necessary and identify by block number*) FEL, undulator, CEBAF, phase velocity,

19 ABSTRACT (*continue on reverse if necessary and identify by block number*)

The development of the free electron laser (FEL) as a source of coherent radiation continues toward the fulfillment of its potential for high power, high efficiency and short wavelength. New ezperiments toward fulfillment of the FEL's potential present new phenomenon to be studied by theoreticians and experimentalists. Two of these phenomenon in short wavelength FELs are the shift in phase velocity resonance and the reduction in gain.

The first part of this thesis presents an argument for the use of the FEL in a maritime military capacity. The advantages of the FEL over conventional kinetic systems and other high-energy laser systems are emphasized.

The remainder of this thesis examines several effects of short wavelength FELs. In particular, Chapter IV examines the characteristics of the proposed CEBAF UV FEL and presents alternative designs to assist in design selection. Chapter V analyses the resonant phase velocity shift and loss in gain that occurs in short wavelength FELs and presents a method to predict the resonant phase velocity and gain.

Chapter VI presents a new tool for examining the optical mode within the FEL. By removing the input optical field from the total optical field , only the excited optical field amplitude and phase remain. Chapter VI presents a modification to a self-consistent three-dimentional simulation that will display the excited optical field.

20 DISTRIBUTION/AVAILABILITY OF ABSTRACT ☒ UNCLASSIFIED/UNLIMITED ☐ SAME AS REPORT ☐ DTIC USERS	21 ABSTRACT SECURITY CLASSIFICATION UNCLASSIFIED	
22a NAME OF RESPONSIBLE INDIVIDUAL W. B Colson	22b TELEPHONE (*Include Area code*) (408) 646-7652	22c OFFICE SYMBOL 61cw

DD FORM 1473, 84 MAR 83 APR edition may be used until exhausted
All other editions are obsolete

SECURITY CLASSIFICATION OF THIS PAGE
UNCLASSIFIED

Approved for public release; distribution is unlimited.

THEORY FOR THE CEBAF AND SHIPBOARD FELS

by

C. A. Bice

Lieutenant, United States Navy

B. BA., University of Notre Dame, 1984

Submitted in partial fulfillment of the

requirements for the degree of

MASTER OF SCIENCE IN PHYSICS

from the

NAVAL POSTGRADUATE SCHOOL

December 1991

Karlheinz E. Woehler, Chairman,

Department of Physics

ABSTRACT

The development of the free electron laser (FEL) as a source of coherent radiation continues toward the fulfillment of its potential for high power, high efficiency and short wavelength. New experiments toward fulfillment of the FEL's potential present new phenomenon to be studied by theoreticians and experimentalists. Two of these phenomenon in short wavelength FELs are the shift in phase velocity resonance and the reduction in gain.

The first part of this thesis presents an argument for the use of the FEL in a maritime military capacity. The advantages of the FEL over conventional kinetic systems and other high-energy laser systems are emphasized.

The remainder of this thesis examines several effects of short wavelength FELs. In particular, Chapter IV examines the characteristics of the proposed CEBAF UV FEL and presents alternative designs to assist in design selection. Chapter V analyzes the resonant phase velocity shift and loss in gain that occurs in short wavelength FELs and presents a method to predict the resonant phase velocity and gain.

Chapter VI presents a new tool for examining the optical mode within the FEL. By removing the input optical field from the total optical field, only the excited optical field amplitude and phase remain. Chapter VI presents a modification to a self-consistent three-dimensional simulation that will display the excited optical field.

1 K0515
B51127
C.1

Table of Contents

I. INTRODUCTION 1

II. THE SHIPBOARD FREE ELECTRON LASER 3

A. MOTIVATION FOR A SHIPBOARD HIGH-ENERGY LASER 3

B. ADVANTAGES OF THE SHIPBOARD FEL 6

C. THEORETICAL FEL RANGE LIMITS 12

D. DISCUSSION 14

III. FREE ELECTRON LASER THEORY 16

A. BASIC FREE ELECTRON LASER PHYSICS 16

B. ELECTRON DYNAMICS AND THE PENDULUM EQUATION 20

C. THE SELF-CONSISTENT WAVE EQUATION 23

D. FEL DIMENSIONLESS PARAMETERS 26

IV. THE CEBAF ULTRAVIOLET FEL DESIGN 28

A. BACKGROUND 28

B. THE CEBAF UV FEL DESCRIPTION 29

C. OPTIMIZING THE CEBAF UV FEL DESIGN 31

D. ALTERNATIVE DESIGNS FOR THE CEBAF UV FEL 39

V. FELS WITH LARGE FILLING FACTOR 42

A. INTRODUCTION 42

B. THE PHASE VELOCITY RESONANCE SHIFT 43

1. The Resonant Phase Velocity 43

2. The Parabolic Electron Distribution 46

3. The Gaussian Electron Distribution 48

C. GAIN DEGRADATION WITH LARGE ELECTRON BEAMS 49

D. DISCUSSION 51

VI. OPTICAL MODE DISTORTION 52

A. INTRODUCTION 52

B. THE NUMERICAL SIMULATION 52

C. THE INPUT OPTICAL FIELD 54

D. THE EFFECT OF BEAM SIZE ON MODE DISTORTION 54

E. THE EFFECT OF GAIN ON MODE DISTORTION 63

F. DISCUSSION 65

VII. CONCLUSIONS 69

LIST OF REFERENCES 71

INITIAL DISTRIBUTION LIST 74

ACKNOWLEDGEMENT

The author gratefully acknowledges the guidance and support of Dr. W. B. Colson. The author also gratefully acknowledges the assistance and endless patience of his loving wife, Penny.

I. INTRODUCTION

The free electron laser (FEL) uses the energy of a relativistic electron beam to produce coherent radiation and promises high power, efficiency and reliability. The FEL was first proposed by John Madey in 1970 [1] and has since been the object of significant research and development efforts at universities, national laboratories and private industry around the world. Theoretical understanding and technological demonstrations of FELs are approaching the full potential of the FEL as a source of coherent radiation.

There are many reasons that such significant interest is being shown in FEL development. Among those reasons are the potential for multi-megawatt average power output, very high wallplug efficiency, and optical wavelength tuneability over an order of magnitude. A system of such potential shows promise for military applications as well as significant medical and scientific research. The military applications which might develop with the maturation of the FEL have been the subject of considerable study. Ground-based as well as space-based FELs have been a topic of interest of the Strategic Defense Initiative Office (SDIO) for quite some time and have been studied extensively. A shipboard FEL (SFEL) is discussed in Chapter II with emphasis on the advantages such a system would have over conventional kinetic energy systems and other high-energy laser (HEL) systems.

Chapter III gives a brief overview of FEL theory as a lead-in for the development of subsequent chapters. In Chapter IV, the ultraviolet (UV) FEL experiment proposed for the Continuous Electron Beam Accelerator Facility (CEBAF) is examined. In particular, the design of a short wavelength FEL

which will take advantage of the CEBAF superconducting radio-frequency (SRF) accelerator is explored in the hope of assisting in the selection of the optimum design. The research presented in this thesis has contributed to the design of the CEBAF FEL. Features discovered here have led to the modification of the proposed CEBAF UV FEL.

A particular characteristic of FELs that attempt operation at shorter wavelengths is that the optical mode and the electron beam tend to be roughly the same size. Chapter V presents new research on this characteristic and its effect on the resonant phase velocity and gain of the FEL system. Simple equations show that as electron beam size increases relative to the optical mode size, the resonant phase velocity of the FEL is reduced. Additionally, a "universal curve" for predicting the gain of an FEL with a small optical mode is presented and described.

Finally, Chapter VI examines the topic of optical mode distortion and presents a new method for examining its characteristics. Here, a numerical simulation is modified to present the stimulated optical field of an operating FEL. This simulation is a tool which may assist in the understanding of the optical field development in an FEL.

II. A SHIPBOARD FREE ELECTRON LASER

A. MOTIVATION FOR A SHIPBOARD HIGH-ENERGY LASER

There are several factors which make the development of a shipboard high-energy laser (HEL) system a logical and possibly essential progression in naval weapons development. Two major factors are the modern threats which face the surface ship battle groups (BGs) and the addition of anti-ballistic missile (ABM) and anti-satellite (ASAT) missions to the missions of sea control and power projection.

In the past decade, quantum advances in the performance of anti-ship missiles (ASMs) have led opponents of surface combatant warfare to conclude that surface ships (and aircraft carriers in particular) are becoming obsolete. These opponents surmise that the advent and proliferation of sophisticated long-range, high-speed, low-flying missiles make protection of BGs so difficult that they are virtually indefensible. Missiles fired from short range or missiles incorporating stealth technology will require a rapid response from a ship's defensive systems.

In an interview for the *Navy Times*, Commander Gregory Dundas, Deputy Head of the Antiair Warfare Division in the office of the Assistant Chief of Naval Operations for Naval Warfare, said, "Ship self-defense is our greatest challenge and most immediate weakness." [3] Quick Reaction Combat Capability (QRCC) is a high-priority program to improve surface ship defense against sea-skimming, antiship cruise missiles. Systems like QRCC will become increasingly important as force reductions take place. The same *Navy Times*

article reported that Navy officials said, "In the future, deployments will be responsible for defending larger areas of the ocean," and Dundas added, "Sea control is a must. We need to do more with a smaller force of ships." [2]

Statements like these demonstrate the need for a more potent naval weapons system. With the additional threat of modern theater or tactical ballistic missiles (TBMs), the argument is even stronger. An HEL, and in particular a free electron laser (FEL), if applied to ASM and TBM defense, would be a quantum improvement over the current QRCC plan, and would be the solution that would enable the fleet to successfully defend itself and continue to carry out its vital missions.

One of the difficulties associated with defending the BG or an individual ship is the time lag between the detection of a threat and its destruction. The most significant part of this time lag is the time between the employment of a defensive surface-to-air missile (SAM) system and the destruction of the threat. In the engagement of a supersonic ASM at long range with modern SAMs this time lag can exceed 2 minutes. Even at short range, the time between the defensive system employment and threat destruction can be more than 10 seconds. In the time it takes a SAM to transit to the ASM, the ASM may have moved more than 3 km closer to the ship and a second shot, if necessary, may not be possible. A weapon that fires lethal energy at the speed of light has a tremendous advantage over kinetic weapons in shoot-look-shoot sequences.

A second difficulty associated with defending a ship or BG is that of limited SAM inventory, known as magazine depth. Due to probability of kill (PK) for each SAM, hostile electronic counter-measures, and deception, it is likely that multiple SAM engagements would be required to destroy each inbound ASM. If

faced with a large, coordinated attack with perhaps dozens of ASMs, a BG could quickly expend all of its available ordnance. The last ditch defense of even the Close In Weapons System (CIWS) is limited to only a few engagements, and even an ASM kill at short range may result in significant damage to the defenders due to debris from the ASM. Therefore, a defensive system which has a limitless supply of "ammunition" has significant advantage over present and projected future defensive missile systems.

The Strategic Defense Initiative (SDI) began in a speech March 23, 1983 when President Ronald Reagan called on the United States scientific community to develop a system which, ". . . could intercept and destroy strategic ballistic missiles before they reach our soil. . . ." [3] High-energy lasers are expected to play an important role in ballistic-missile defense (BMD) and FELs, as well as excimer lasers, are the most attractive candidates for this mission [3]. As a part of SDI, FELs were proposed as HELs that could be used as ASAT weapons or as a defense against intercontinental ballistic missiles (ICBMs). Many organizations have worked to develop a space-based FEL (SBFEL) concept including Los Alamos National Laboratory, Lawrence Livermore National Laboratory, TRW, and the Lockheed Missile and Space Company. One such concept was developed by Lockheed under contract to the Air Force Space Division [4]. A TRW point paper suggested that the capabilities and technology required of the SBFEL could be adapted to the Ship Missile Defense FEL (SMDFEL) concept [5]. A combination of the SBFEL and SMDFEL concepts could fulfill significant needs of the Navy including fleet defense against strategic and tactical aircraft, cruise and tactical anti-ship missiles and tactical ballistic missiles.

A concept presented to the Physics department of the Naval Postgraduate School by Lieutenant Colonel Ed Pogue, USA, former Deputy Director of Directed Energy for the Strategic Defense Initiative Office, coupled a shipboard FEL with a high-altitude mirror relay. This concept, named Thunderball, was studied by Jim Bell of the Advanced Technology Group of W. J. Schafer Associates. [6] The high-altitude relay would provide for the additional missions of cueing and designation for ground-based kinetic energy weapons, contingent theater defense against theater ballistic missiles, tactical satellite interdiction, and limited or full global protection against limited strikes (GPALS) [6].

B. ADVANTAGES OF THE SHIPBOARD FEL

There are many characteristics that make the SFEL a logical choice for development as a naval weapon. Among these characteristics are the speed-of-light delivery of lethal energy, the relatively infinite magazine, the short and tuneable wavelength, the high power scalability, and the very high efficiency.

The speed of light is the fastest possible speed for the delivery of any type of lethal energy. The speed of light delivery of lethal energy by an HEL would greatly reduce the time lag associated with the time of flight of SAMs. In either an offensive or defensive role, a light-speed weapon could rapidly engage many targets in a very short time and, with continuous engagement, would have a high PK. As an example, suppose an ASM traveling at Mach 2 is detected and identified by a ship at a range of roughly 10 km. From the time of launch, a SAM traveling at Mach 2.5 would require about 7 seconds to intercept the incoming ASM. By this time, the ASM would be within 5 km. After the estimated time of intercept, an assessment of kill or miss would have to be

made before a re-engagement could be attempted. If the shot was evaluated as a miss, a second SAM would have to be fired or, if the target was at very short range, the CIWS would have to be engaged. Realistically, there is no time remaining for re-engagement and a kill by CIWS at such a close range would probably result in damage to the ship. In contrast, the use of a light-speed weapon would require about zero transit time (roughly 0.3 μs). Depending on the HEL design, the laser dwell time for destruction could be as short as one second, and the HEL could continue to engage the target until the target is evaluated as destroyed. There is virtually no delay between ASM engagement and destruction.

The all-electric nature of the SFEL complements the Navy's integrated electric drive (IED) concept for the all-electric ship of the future. For instance, an FEL with 1 MW average power operating at 25% wallplug efficiency would require 4 MW of prime electrical power. An IED design created by General Electric [7] utilizes two LM2500 gas turbines that deliver power to two propulsion generators. Each generator is rated at 22,187 KVA or 22.2 MW. A provision is also made for two 2500 KW propulsion derived ship service (PDSS) generating systems. Thus, this dual or twin turbine system produces a total electrical power of 49.4 MW and operates at 93.6% efficiency. With larger systems (for instance four rather than two gas turbines and associated equipments) the total output power of 98.8 MW is very feasible. Although this would require a larger ship to accommodate the larger engineering plant, the technology is definitely scalable. For instance, the Spruance class destroyers and the more modern Ticonderoga class cruisers currently used in the Navy operate with marine gas turbine propulsion plants with four LM2500 gas turbines. These ships also use several smaller marine gas turbine electrical

generators. The addition of superconducting technology to the IED system provides potential for even greater power outputs and efficiencies. Because the FEL is an all-electric system, it has the advantage of having a virtually limitless supply of "ammunition". The FEL depends only on the amount of fuel a ship can carry to maintain a steady supply of electrical power not a magazine of "bullets" or weapon specific chemicals like a CO_2 laser.

An FEL's optical wavelength is governed by the resonance condition [8]

$$\lambda = \lambda_0 \frac{(1 + K^2)}{2\gamma^2} \qquad 2\text{-}1$$

where λ_0 is the undulator wavelength, K is the undulator parameter and γ is the electron beam Lorentz factor. A broad range of wavelengths and easy tuneability are two factors that set FELs apart from conventional lasers that are tied to the natural resonance frequency of the atom or molecule. An FEL can be designed to operate in any wavelength band from nm to mm by selecting an appropriate undulator wavelength and electron beam energy. An FEL can be designed to take advantage of a wide range of wavelengths. It is possible to design an undulator with a range of undulator wavelengths available and it is fairly simple to alter the energy of the driving electron beam and thus the Lorentz factor. It is also possible and quite simple to adjust the undulator magnetic field, and thus the undulator parameter, to tune an operating FEL to a very specific wavelength. FELs have demonstrated operation from 240 nm to 18 mm and have demonstrated continuous tuneability of a single FEL over the operating wavelength by a factor of 10 [8]. The FEL can therefore be designed to adapt to new understanding of the most favorable atmospheric transmission band and counter-measures, and can be tuned to account for local

atmospheric variations to obtain optimum transmission. Still, atmospheric propagation at low altitudes may be the most difficult obstacle for the application of FELs to naval missions.

The absorption of optical radiation by the atmosphere is dependent upon wavelength in a very complex manner. This absorption leads to thermal blooming. Fortunately, there exist certain wavelength regions with low atmospheric absorption. A calculated, high-resolution, atmospheric transmission spectrum at 3.8 μm over 10 km sea level path at 0°C and 76% relative humidity shows transmittance of better than 95% [9]. Transmission at 3.8 μm would minimize the effects of thermal blooming. Though aerosol and turbulence effects become dominant and lead to large variations in performance at the shorter wavelengths, the 3.8 μm wavelength offers the best performance. At longer ranges performance can be improved by using multiple-pulse propagation as well as active or adaptive optics techniques for turbulence compensation and for thermal blooming correction. [10]

The potential for high power in an FEL has been demonstrated by several experiments, but the most important characteristic of a weapons grade FEL, high-average power, has yet to be demonstrated over long periods of time. To date, average powers of only a few watts have been observed in several experiments [8].

The typical FEL optical output consists of a macropulse made up of a train of short, high-power micropulses. This macropulse and train of micropulses are a direct result of the pulsed electron bunches input to the FEL undulator from the accelerator. The average power of the macropulse is determined by the peak pulse power, the pulse length and the micropulse repetition frequency. The average power of the FEL is determined by the average macropulse power

and the macropulse repetition frequency. While high peak power and high micropulse repetition frequency have been demonstrated, the technology for a continuous train of micropulses is still being investigated. The Continuous Electron Beam Accelerator Facility (CEBAF) UV and IR FEL experiments will demonstrate continuous electron micropulses and high average power [11].

High peak power has been demonstrated in several FEL experiments. The ELF II microwave FEL at Lawrence Livermore National Laboratory (LLNL) was able to produce 1 GW peak powers over 50 ns pulses [12]. The Los Alamos FEL produced peak intercavity power of 2 GW with peak output power of 40 MW over 16 picosecond micropulses at 10 μm wavelength [13]. Neither of these facilities, however, have been able to demonstrate the continuous micropulse repetition frequency necessary for high average powers.

To date the highest average power achieved is 10 W produced by the superconducting accelerator (SCA) FEL experiment at Stanford [8]. The SCA experiment used 5 ps duration micropulses at 12 MHz with 100 μs duration macropulses at 20 Hz. This average power was achieved with peak power of only 1MW. The proposed CEBAF UV FEL may demonstrate average power at least 2 orders of magnitude higher [11]. With a continuous train of 1 ps pulses at 7.5 MHz and peak power of 480 MW, the CEBAF UV FEL should demonstrate average powers near 4 kW. Continued research into superconducting RF accelerators will probably produce even greater results.

The wallplug efficiency of an FEL will be defined as the average optical power output of the FEL divided by the prime electrical power input. The extraction efficiency of an FEL is the fraction of the electron beam power that is converted into optical power in one pass through the undulator. While the output power of the laser depends upon the extraction efficiency of the FEL

undulator, the wallplug efficiency is more dependent upon superconducting technology and electron beam recirculation. Both TRW and CEBAF estimate that wallplug efficiency could be as high as 40%. The development of superconducting radio frequency (SRF) accelerators has proven to be a huge technological achievement. SRF accelerators provide the capability to accelerate higher peak and average electron currents which in turn provide high gain and high-average optical power. Additionally, the high Q of the cavities means there are few losses as the electrons are accelerated by the RF field.

The development of energy recovery by RF accelerators is very exciting. By recirculating the electron beam through a decelerating mechanism after the beam has passed through the undulator, much of the kinetic energy of the electrons is converted back into RF energy for the accelerating cavities. Much of the energy which remains in the electron beam after passing through the undulator is not lost to a beam dump. The Los Alamos National Laboratory (LANL) FEL used a resonant bridge coupler to pass RF energy from a set of decelerating cavities back to the accelerating cavities [14]. The accelerated electron beam was passed through a FEL undulator where 0.7% of the energy was converted into optical power. The electron beam was then passed through a series of decelerating cavities where 68% of its energy was converted back into RF power. A similar system in which the electron beam is introduced into the original accelerating cavities with an approximate 180° phase shift may be even more efficient.

The ability to recover energy from the electron beam is dependent upon the electron beam characteristics. These characteristics are in turn dependent upon the accelerator injector, the FEL undulator and the electron beam transport system. If more of the energy is extracted from the electron beam in

the undulator, it becomes more difficult to recover RF power from it. At LANL, lasing with about 1% extraction efficiency did not degrade the energy recovery. Overall, extraction efficiency of more than 5% with energy recovery of 70% in SRF accelerators should lead to high average power laser operations with greater than 40% wallplug efficiencies.

C. THEORETICAL FEL RANGE LIMITS

In order to establish the range limitations of a shipboard FEL, assumptions were made based on the best available information. In the case of the SFEL, the primary assumptions involved the required flux on target and especially on atmospheric propagation of high-power lasers. The information available which describes the required flux on target varies from 1 kJ/cm^2 to 100 kJ/cm^2. Assuming an energy flux of 10 kJ/cm^2, whch corresponds to a power density on target of 10 kW/cm^2 over 1 second, accounts for some target hardening.

In combining the SMDFEL and Thunderball concepts into a single SFEL concept, it becomes apparent that there are two distinct modes or mission profiles. The first is direct defense against an incoming threat and the second is long-range intercept of a threat through a high altitude relay. In the direct defense mode, the SFEL engages the inbound aircraft or missile with no relay and the light must transit to the target near the surface. For threats at very low altitudes, the engagement range is limited to the horizon distance [15]

$$\text{Range (km)} \approx 3.71 \times \sqrt{\text{Height (m)}} \quad ,$$

where the height is the sum of the director and the target heights. For instance, a SFEL system with beam director height of 20 m engaging an incoming target at 6 m is limited to a horizon range of about 19 km. This distance will be

extended for targets at higher altitudes, but is limited by beam director height for very low altitude missiles. In this direct defense mode, the optical beam must propagate near the sea surface where the propagation effects of attenuation and thermal blooming are most severe.

A spot size (diameter) on target of 10 cm balances the requirement to keep power density high while staying within limits of pointing and tracking accuracy at long ranges to achieve the necessary dwell time. The beam director diameter required to focus to a 10 cm spot at 20 km is a direct result of diffraction limited beam so that

$$D = R\lambda\sqrt{\pi/A} = R\lambda/r^2 = (20\ km)(3.8x10^{-6}\ m)/.05\ m = 1.5\ m.$$

For higher altitude target, range is limited by ability to focus the diffraction limited beam to a 10 cm spot with a given beam director size. Given a reasonable director size of 3 m the maximum range is determined by [3]

$$R^2 = AD^2/\pi\lambda^2 \quad ,$$

$$R = rD/\lambda \approx 40km \quad . \qquad 2\text{-}2$$

The average laser output power required to deliver 10 kJ/cm^2 over a 10 cm spot at 40 km comes from the equation for fluence [3]

$$F = PtD^2/\pi R^2\lambda^2 \quad ,$$

so that

$$P = \pi FR^2\lambda^2/tD^2 \approx 807kW \quad . \qquad 2\text{-}3$$

Assuming a maximum of 25% transmission, including beam blowup losses, the required FEL output is about 3.2 MW.

There are many options available for a high-altitude relay system to extend ranges against high-altitude targets. Placing a relay mirror at 80,000 ft (25 km) avoids the most significant portions of the atmosphere and significantly improves laser propagation and the lethal range [6]. A larger output mirror at this high altitude would allow focusing over much greater distances. In this case, maximum lethal range is limited by laser output power and output mirror diameter. If the maximum power output is limited to 10 MW then, neglecting mirror and transmission losses, a maximum range for high altitude intercept can be calculated. Assuming a 6 m relay mirror and a 3 m beam director, with the same fluence required on target, the maximum range becomes [3]

$$R^2 = PtD^2/\pi F\lambda^2 \quad ,$$

$$R = \sqrt{Pt/\pi F}\, D/\lambda \approx 300 km \quad . \qquad 2\text{-}4$$

To get the laser power up to the high altitude relay requires the ability to focus the ship's output to a size smaller than the input mirror of the relay. Because the laser output beam is nearly diffraction-limited, the minimum spot size is determined by range, wavelength and director diameter. A 3.8 μm laser with a 3 m director can easily focus on a 3 m input mirror for the relay at 25 km.

D. DISCUSSION

The need for a very fast and effective defensive system for ships and battle groups has been amply demonstrated. Additionally, the Navy's capabilities must grow to meet the needs of the new ASAT and ABM missions. It is therefore essential that long term research be devoted to develop FELs and

demonstrate their full potential. While there are still many technological roadblocks to the deployment of the FEL as a weapons system, the proven advantages, the scalability, and the potential efficiency make the FEL a logical choice for development.

III. FREE ELECTRON LASER THEORY

A. BASIC FREE ELECTRON LASER PHYSICS

An FEL consists of two major components. An electron accelerator provides a stream of relativistic electron bunches to an undulator which has a periodic magnetic field to "wiggle" the electrons as they pass. The periodic acceleration of the electrons causes them to radiate in a forward cone. Some of this spontaneous radiation may be saved in a laser resonator formed by placing two curved mirrors beyond the ends of the undulator. As the radiation builds, the coupling of the optical field in the undulator with the wiggling electron beam leads to stimulated emission and coherent radiation. Though this is a quantum description of the electron/optical field interaction, FELs can be described as classical devices and may be described with electro-magnetic theory [16].

The radio-frequency (RF) electron accelerator yields picosecond long bunches of electrons with peak current on the order of one to hundreds of amps. The electron bunches achieve typical energies, $(\gamma - 1)mc^2$, of tens of MeVs up to hundreds of MeVs giving Lorentz factors on the order of $\gamma = 10^2$. The radius of the electron beam is generally on the order of millimeters and yields an electron density on the order of $\rho = 10^{12} - 10^{13}\ cm^{-3}$. The beam quality, described in terms of the energy spread and emittance, can have a large effect on FEL gain. Energy spread is the spread in the electron velocities described by $\Delta\gamma/\gamma$. Emittance $\varepsilon = r\,\bar{\theta}$ where r is the rms initial position spread of the electrons and $\bar{\theta}$ is the rms initial angular spread. While the position and

angular spreads of the electrons can be changed in the beam transport system of the accelerator, the emittance remains constant [17]. The normalized emittance, $\varepsilon_n = \gamma \varepsilon$, is useful in comparing the beam quality of accelerator at different energies. Typically, each electron bunch has a spread in electron energies of a few tenths of a percent and a normalized emittance on the order of a few to a hundred mm-mrad.

The undulator consists of a periodic magnetic field with linear or helical polarization. The magnetic field may be generated by permanent magnets, current-carrying coils, or a combination of each. Each undulator period, λ_0, is typically a few centimeters long with perhaps N=100 periods giving the undulator a length on the order of a few meters. The strength of the undulator may be described by the undulator parameter $K = e\bar{B}\lambda_0/2\pi mc^2$ where e=|e| is the charge magnitude of an electron, m is the mass of an electron, and c is the speed of light. The rms magnetic field strength $\bar{B} = B/\sqrt{2}$ is typically a few kilogauss so that $K \approx 1$.

The electron beam transverse dimension and angular spread contribute to the line width of the FEL. The spread in the line width is minimized when the contribution of the radial spread is equal to the contribution of the angular spread. The equal contributions leads to the optimum condition for focusing the electron beam as [17] $Kk_0r_e = \gamma\bar{\theta}$, and leads to a matching beam radius of $r_e = \sqrt{\varepsilon_n\lambda/\sqrt{2}\pi K}$. This matching condition gives smooth propagation of the electron beam along the undulator axis with minimum spread in the line width. As the number of undulator periods increases and the optical wavelength decreases the FEL becomes more sensitive to emittance.

Figure 3-1 shows the microscopic features of the classical approach to FEL physics. At the top of Figure 3-1, electrons enter the undulator and encounter the periodic magnetic field where they begin to oscillate. As the electrons oscillate they emit photons in a forward cone. The middle of Figure 3-1 shows one period of the undulator expanded. The radiation travels along the undulator over one period of the undulator magnetic field as the electron follows a sinusoidal path over the same undulator period. The bottom of Figure 3-1 shows that the effect of the optical field on the electron is dependent on the relative phase between the electron and the optical field. When the electron has a velocity component in the z direction (along the undulator axis) it may experience a retarding or an accelerating force that causes the electron to give up or gain energy. Because energy conservation must apply, the energy given up by an electron is stored in the optical wave leading to amplification of the optical field. The energy can be absorbed by an electron depending on the phase between the electron and the optical wave. Then, the optical field gives energy to the electron resulting in a loss in the optical field and acceleration of the electron.

In an initially random beam, spread over many optical wavelengths, both absorption and loss occur in roughly equal amounts. At a particular wavelength, the energy transfer to the optical field can be made to dominate giving rise to net gain [16].

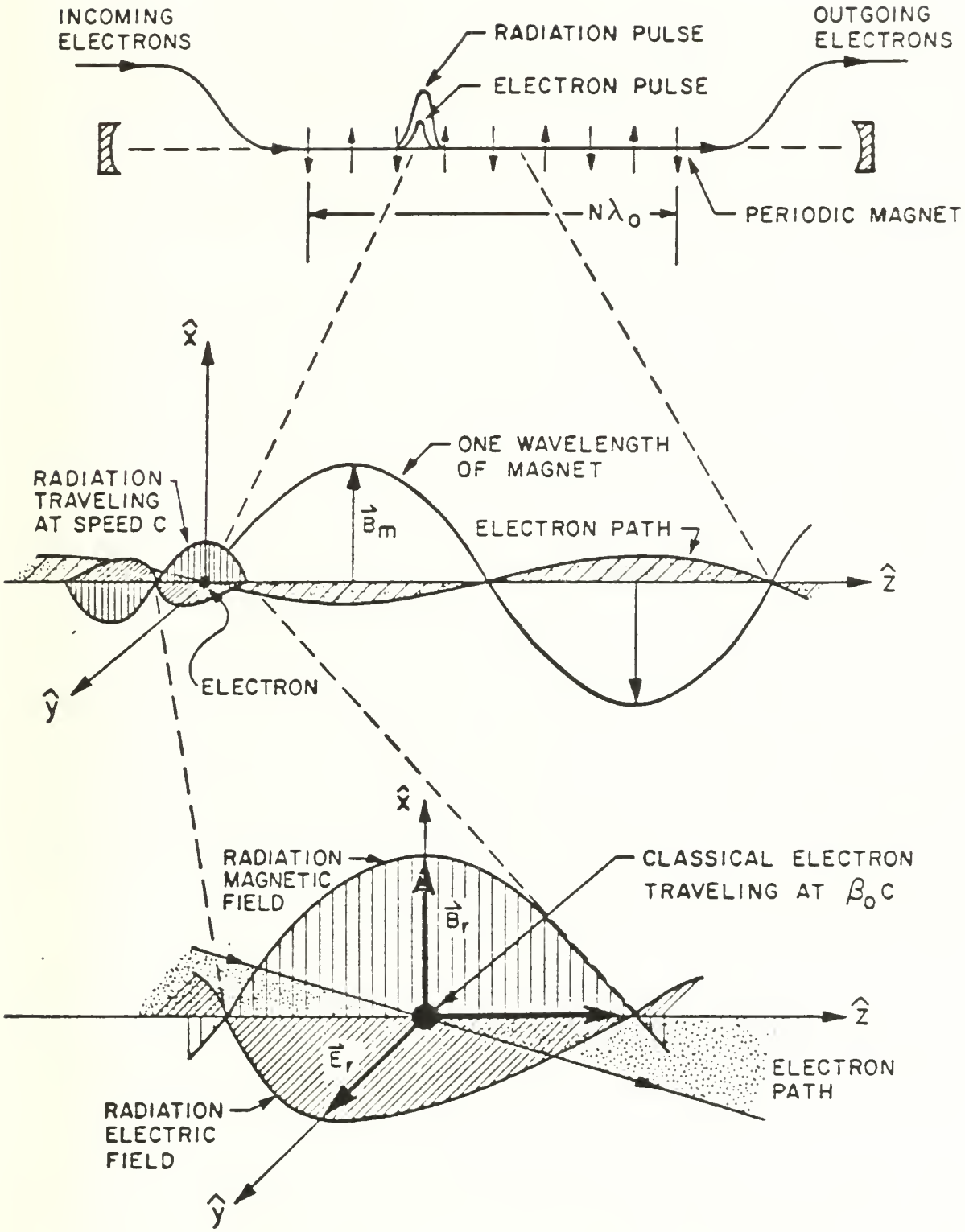

Figure 3-1: Major components of the FEL illustrating the fundamental physics of the laser.

B. ELECTRON DYNAMICS AND THE PENDULUM EQUATION

The forces acting on the electron in the undulator are governed by the relativistic Lorentz force

$$\frac{d(\gamma\vec{\beta})}{dt} = -\frac{e}{mc}(\vec{E}_r + \vec{\beta}\times(\vec{B}_r + \vec{B}_u),\ \dot{\gamma} = -\frac{e}{mc}(\vec{\beta}\cdot\vec{E}_r),\ \gamma^{-2} = 1-\vec{\beta}\cdot\vec{\beta} \quad , \qquad 3\text{-}1$$

where $\vec{v} = \vec{\beta}c$ is the velocity of the electron, $\vec{E}_r = E[\cos\psi,-\sin\psi,0]$ and $\vec{B}_r = E[\sin\psi,\cos\psi,0]$ are the electric and magnetic fields of the optical wave and $\vec{B}_u = B[\cos(k_0z),\sin(k_0z),0]$ is the undulator magnetic field for a helically polarized undulator. Equations for the trajectories of the electrons in the undulator are derived by inserting the equations for the electric and magnetic fields into equation 3-1. Because there are five component equations in equation 3-1 and only four unknowns $[\vec{x}(t), \gamma(t)]$, one of the component equations can be ignored. When $v \approx c$, $\beta_z \approx 1$ and $z(t) \approx \beta_0 ct + ...$ and the electrons travel mainly along the axis of the undulator. In this case, the transverse optical fields in the first equation nearly cancel so that the transverse optical force is much less than the undulator field force, $|E_r|(1-\beta_z) \ll \beta_z B$ [16]. When this is the case, the transverse force on the electrons is primarily determined by the undulator field and the transverse component of equation 3-1 becomes

$$\frac{d}{dt}(\gamma\beta_\perp) \approx -\frac{e}{mc}\beta_z B[-\sin(k_0z),\cos(k_0z),0] \quad . \qquad 3\text{-}2$$

The transverse velocity of the electrons is found by integrating equation 3-2 by inspection. The result is

$$\vec{\beta} = -\frac{K}{\gamma}[\cos(k_0z),\sin(k_0z),0] \quad , \qquad 3\text{-}3$$

where $K = eB\lambda_0/2\pi mc^2$ is again the undulator parameter. The constants of integration have been eliminated by assuming perfect beam injection.

Integrating once more yields the trajectories of the electrons in the undulator as

$$\vec{X}_{\perp} \approx \frac{\lambda_0 K}{2\pi\gamma}[-\sin(\omega_0 t),\cos(\omega_0 t),0] \quad , \qquad 3\text{-}4$$

where $\omega_0 = k_0 c$. Because $\gamma \gg 1$ and $K \approx 1$, the transverse oscillations are small ($\Delta x/\lambda_0 \approx K/2\pi\gamma$) compared to the undulator wavelength.

Because the magnetic field increases off-axis, a second, slower oscillation called betatron motion is superimposed on the oscillation of the electrons in one period of the undulator. The wavenumber of this motion is $k_\beta = Kk_0/\gamma$. This motion is characteristic of the natural focusing of the undulator field [16]. The number of betatron oscillations is $N_\beta = k_\beta L/2\pi = KL/\gamma\lambda_0 = KN/\gamma$. If N_β is small, there is no significant focusing in the FEL. [16]

The laser gain can be calculated from the second equation of equation 3-1 as the change in energy $d\gamma/dt = \dot{\gamma}$. Substituting the optical electric field $\vec{E}_r$ into equation 3-1 gives

$$\dot{\gamma} = -\frac{e}{mc}(\vec{\beta}_{\perp}\cdot\vec{E}_r) \quad , \qquad 3\text{-}5$$

because $E_z = 0$. Now,

$$\frac{\dot{\gamma}}{\gamma} = \frac{eEK}{\gamma^2 mc}\cos(\zeta + \phi) \quad , \qquad 3\text{-}6$$

where $\zeta = \zeta(t) = \psi + k_0 z(t) = (k + k_0)z(t) - \omega t$ becomes the electron phase. At t=0, $\zeta(0) = \zeta_0 = (k + k_0)z_0$. Because $k \gg k_0$, $\zeta_0 \approx kz_0 \approx 2\pi z_0/\lambda$. The electron phase relates the electron z position to the optical wavelength.

To find the evolution of the electrons in the presence of an optical field, the Lorentz factor is written in terms of the electron phase using the fact that $\gamma^{-2} = 1-\vec{\beta}^2 = 1-\beta_{\perp}^2-\beta_z^2$ and $\beta_{\perp} = K/\gamma$. When γ is large, $\beta_z \approx 1-(1+K^2)/2\gamma^2$. Taking

derivatives of the electron phase,

$$\dot{\zeta} = (k+k_0)\dot{z} - \omega \approx k_0\beta_z c - k(1-\beta_z)c \quad , \qquad 3\text{-}7$$

and

$$\ddot{\zeta} = (k+k_0)\ddot{z} = kc\frac{(1+K^2)}{\gamma^2}\frac{\dot{\gamma}}{\gamma} \quad ,$$

$$\ddot{\zeta} = kc\left[\frac{1+K^2}{\gamma^2}\right]\frac{eEK}{\gamma^2 mc}\cos(\zeta+\phi) \quad . \qquad 3\text{-}8$$

Because $\omega(1+K^2)/2\gamma^2 = \omega_0 = k_0 c$ equation 3-8 can be written as

$$\ddot{\zeta} = \frac{2eEKk_0}{\gamma^2 m}\cos(\zeta+\phi) \quad .$$

The dimensionless time can now be defined as $\tau = ct/L$ so that $\tau = 0 \rightarrow 1$ as the electrons pass down the undulator. Now, $d(..)/dt = (L/c)\, d(..)/d\tau = \overset{\circ}{(..)}$, and $d^2(..)/dt^2 = (L/c)^2 d^2(..)/d\tau^2 = \overset{\circ\circ}{(..)}$ so that the pendulum equation can be written as

$$\overset{\circ\circ}{\zeta}(\tau) = \frac{L^2}{c^2}\frac{2eEKk_0}{\gamma_0^2 m}\cos(\zeta+\phi) = |a|\cos(\zeta+\phi) \quad , \qquad 3\text{-}9$$

where $|a| = 4\pi NeEKL/\gamma_0^2 mc^2$ is the dimensionless optical field strength. Equation 3-9 is the pendulum equation which describes the evolution of the electrons through the undulator. In equation 3-9, if $-3\pi/2 < (\zeta+\phi) < \pi/2$ the electrons will lose energy to the optical field. Similarly, if $\pi/2 < (\zeta+\phi) < 3\pi/2$ the electrons will gain energy from the optical field.

If the electron phase velocity is defined as $\nu = \overset{\circ}{\zeta}$, and the equation for ζ above is used, in dimensionless form $\nu(\tau) = L[(k+k_0)\beta_z - k]$. The electron phase velocity is a measure of the resonance between the electron beam, the undulator, and the optical field. If $\nu(\tau) = 0$, then the FEL is at resonance and $k = (k+k_0)\beta_z$ and $k = k_0\beta_z/1-\beta_z$. Because $\beta_z = 1-(1+K^2)/\gamma^2 \approx 1$ for $\gamma >> 1$, then

$k \approx 2\gamma^2 k_0/(1+K^2)$ and the resonant wavelength is

$$\lambda = \frac{\lambda_0(1+K^2)}{2\gamma^2} \quad . \qquad 3\text{-}10$$

Equation 3-10 shows that the resonant operating wavelength of an FEL can be altered by changing the electron beam energy $(\gamma-1)mc^2$, the undulator wavelength λ_0, or the undulator parameter K.

C. THE SELF-CONSISTENT WAVE EQUATION

Maxwell's wave equation can be used to describe the optical evolution in an FEL. Spontaneous emission in an FEL oscillator grows to form a classical wave with a bandwidth comparable to the inverse of the number of undulator periods, $1/N$ [16]. This means that the wave has some degree of coherence even after one pass. The narrow bandwidth of the laser allows the assumption that the optical wave varies slowly in space over one optical wavelength ($E' << kE$, $\phi' \ll k\phi$). This is the slowly-varying amplitude and phase approximation (SVAP). This can be viewed as a carrier wave of a single frequency which is modulated by a complex wave envelope that is slowly-varying in amplitude and phase over many optical wavelengths.

Neglecting transverse effects of the optical field, it can be assumed that a circularly-polarized plane-wave which is present in the undulator has a vector potential of the form

$$\vec{A} = \frac{E(t)}{k}[\sin\psi, \cos\psi, 0) \quad , \qquad 3\text{-}11$$

where $E(t)$ is the optical electric field, k is the optical wavenumber and $\psi = kz-\omega t+\phi$. Using the vector potential in Maxwell's wave equation [16]

$$\left[\vec{\nabla}^2 - \frac{1}{c^2}\frac{\partial^2}{\partial t^2}\right]\vec{A} = -\frac{4\pi}{c}\vec{J}_t \quad , \qquad 3\text{-}12$$

where $\vec{J}_t$ is the transverse current from the transverse motion of the electron beam in the Coulomb gauge [16]. The SVAP is used to eliminate all spatial terms with two derivatives or higher to get

$$\left[\vec{\nabla}^2 - \frac{1}{c^2}\frac{\partial^2}{\partial t^2}\right]\vec{A} \approx \frac{2}{c}\frac{\partial E_r}{\partial t}[\cos\psi, -\sin\psi, 0] - \frac{2E_r}{c}\frac{\partial \phi}{\partial t}[\sin\psi, \cos\psi, 0] = \frac{4\pi}{c}\vec{J}_t. \qquad 3\text{-}13$$

The fast rotation of the sine and cosine functions of ψ can be eliminated by defining two orthogonal unit vectors, $\hat{\epsilon}_1 = [\cos\psi, -\sin\psi, 0]$ and $\hat{\epsilon}_2 = [\sin\psi, \cos\psi, 0]$. By projecting equation 3-13 onto $\hat{\epsilon}_1$ and $\hat{\epsilon}_2$, Maxwell's wave equation becomes two first-order scaler equations,

$$\hat{\epsilon}_1 \cdot \left[\vec{\nabla}^2 - \frac{1}{c^2}\frac{\partial^2}{\partial t^2}\right]\vec{A} \approx \frac{2}{c}\frac{\partial E_r}{\partial t} = -\frac{4\pi}{c}\vec{J}_t \cdot \hat{\epsilon}_1 \quad , \qquad 3\text{-}14$$

and

$$\hat{\epsilon}_2 \cdot \left[\vec{\nabla}^2 - \frac{1}{c^2}\frac{\partial^2}{\partial t^2}\right]\vec{A} \approx \frac{2E_r}{c}\frac{\partial \phi}{\partial t} = -\frac{4\pi}{c}\vec{J}_t \cdot \hat{\epsilon}_2 \quad . \qquad 3\text{-}15$$

The single-particle current is $\vec{J}_t = -ec\vec{\beta}\delta^3(\vec{x} - \vec{r}_i)$ where $\vec{r}_i$ is the position of the i^{th} electron and $\delta^3(\vec{x} - \vec{r}_i)$ is the three-dimensional Dirac delta-function [18]. A volume element, dV, which is much smaller than the coherence volume but much larger than the optical wavelength, is selected. By substituting the single-particle transverse current into equations 3-14 and 3-15 and summing over all the particles and averaging both equations at a fixed time over dV [16], equations 3-14 and 3-15 become,

$$\frac{1}{c}\frac{\partial E_r}{\partial t} = -\frac{2\pi e K \rho}{\gamma}\langle\cos(\zeta + \phi)\rangle \quad , \qquad 3\text{-}16$$

and

$$E_r \frac{1}{c}\frac{\partial \phi}{\partial t} = \frac{2\pi e K \rho}{\gamma} \langle \sin(\zeta + \phi) \rangle \quad , \qquad 3\text{-}17$$

where ρ is the electron particle density and <..> represents the ensemble average over all the electrons. Equations 3-16 and 3-17 are simplified by introducing the dimensionless current $j = 8N(e\pi KL)^2\rho/\gamma^3 mc^2$ [16]. With the dimensionless current and the dimensionless field strength, equations 3-16 and 3-17 simplify to

$$\dot{|a|} = -j\langle \cos(\zeta + \phi) \rangle, \quad \dot{\phi} = \frac{j}{|a|}\langle \sin(\zeta + \phi) \rangle \quad , \qquad 3\text{-}18$$

or in phasor form

$$\dot{a} = -j\langle e^{-i\zeta} \rangle \quad , \qquad 3\text{-}19$$

where $a = |a|e^{i\phi}$ is the complex dimensionless field. Equations 3-18 and 3-19 show that the bunching of electrons in phase at $\zeta = \pi$ drives the optical amplitude and leads to gain. While the optical phase $\phi(\tau)$ is driven when the electrons are bunched at $\zeta = \pi/2$. Growth of the optical wave increases with j and is dependent upon the electron distribution <..>. Usually the electron bunching is not perfect and drives both the optical amplitude and phase.

In reality, the evolution of the optical wave in the FEL can be significantly affected by transverse effects such as diffraction. To include transverse effects, the three-dimensional FEL wave equations are derived similar to equations 3-18 and 3-19 from the parabolic wave equation [19] and becomes

$$\left[-\frac{i}{4}\vec{\nabla}^2 + \frac{\partial}{\partial\tau}\right] a(\vec{x},\tau) = -\langle je^{-i\zeta}\rangle \quad . \qquad 3\text{-}20$$

Equation 3-20 can be used to perform numerical integration to simulate an FEL including the effects of beam size, beam quality, and diffraction.

D. FEL DIMENSIONLESS PARAMETERS

Dimensionless parameters are useful in discussing and comparing the attributes of a particular FEL. Several FEL dimensionless parameters have been defined including the undulator parameter, K, the electron phase and phase velocity, ζ and ν, and the optical field strength, $|a|$. There are several more FEL dimensionless parameters which are useful.

When discussing the sizes of the optical mode and the electron beam, it is useful to compare their dimensionless parameters. All transverse dimensions in the FEL are normalized by $\sqrt{\pi/L\lambda}$. The dimensionless electron beam radius is $\sigma_e = r_e\sqrt{\pi/L\lambda}$.

The Rayleigh length, Z_0, is a measure of the optical beam diffraction and is determined by the optical cavity configuration including the mirror curvature and separation. The optical mode waist, W_0, is related to Z_0 by $\pi W_0^2 = \lambda Z_0$. The dimensionless Rayleigh length is $z_0 = Z_0/L$ [17]. When the transverse mode radius is normalized $w_0 = W_0\sqrt{\pi/L\lambda} = \sqrt{Z_0\lambda/\pi}\ x\ \sqrt{\pi/L\lambda}$, so that $w_0 = \sqrt{z_0}$.

The slippage distance, Δs, is the distance the light passes over the electron bunch as the electrons travel down the undulator. Comparing the difference between the distance traveled by an electron and one wavelength of light over one pass down the undulator shows that $\Delta s = \Delta v\ \Delta t = (c-\beta_z c)\ L/c = (1-\beta_z)L = (1-\beta_z)N\lambda_0$. Because $(1-\beta_z) = (1+K^2)/2\gamma^2$ and $\lambda = \lambda_0(1+K^2)/2\gamma^2$, then

$\Delta s = N\lambda$ is the slippage distance. It is the characteristic length over which the electron and light can exchange energy during one pass. If the electron pulse length is much larger than the slippage distance, each part of the optical pulse experiences gain proportional to the local electron density.

IV. THE CEBAF ULTRAVIOLET FEL DESIGN

A. BACKGROUND

The Continuous Electron Beam Accelerator Facility (CEBAF) under construction in Newport News, Virginia is designed to serve as a world center for nuclear physics with the first operation of the full accelerator scheduled to begin in 1994 [11]. The Southeast Universities Research Association (SURA) manages CEBAF under the Department of Energy (DOE). For nuclear physics experiments, the electron accelerator will use superconducting radio-frequency (SRF) cavities to accelerate electron bunches of approximately 0.3 pC charge at a repetition rate of roughly 1.5 GHz. CEBAF will have the capability to deliver simultaneous electron beams of energies 0.8 GeV to 4 GeV to three separate experimentation halls. Parallel to these electron beams, CEBAF proposes to provide accelerated electron beams for use in an infrared (IR) and an ultraviolet (UV) FEL. These FEL experiments provide an excellent step in the technological development of high-efficiency, high-power FELs. To assist in the selection of a design for the CEBAF UV FEL, reference [20] was prepared for the 14th International Free Electron Laser Conference.

CEBAF provides an superb power source for a UV FEL oscillator. [11] The electron beam energy is $(\gamma-1)mc^2 = 400$ MeV where m is the electron mass, c is the speed of light, and $\gamma = 748$ is the Lorentz factor. The continuous train of electron micropulses is 1 ps long with peak current 120 A, energy spread $\Delta\gamma/\gamma \approx 0.002$, and normalized emittance $\varepsilon_n \approx \gamma\,\varepsilon \approx 15$ mm-mrad.

The design of any short wavelength FEL requires addressing problems that originate primarily from limited electron beam quality. The specific features of the CEBAF UV FEL are typical of other short wavelength FELs. The optical mode waist area is proportional to the optical wavelength, λ. When λ is small, the optical mode area tends to be small, and can be smaller than the electron beam. The electrons outside the optical mode do not participate in the gain process and are wasted. The electron beam is limited in size because of finite emittance. This chapter examines and evaluates the performance of the proposed CEBAF UV FEL with recommended deviations from the ususal design criteria [11] in order to optimize gain [20].

B. THE CEBAF UV FEL DESCRIPTION

The basic undulator for the CEBAF UV FEL is linearly-polarized with a wavelength of $\lambda_0 = 6$ cm over $N = 50$ periods and length $L = N\lambda_0 = 3$ m. Electromagnetic coils provide the peak undulator field of $B \approx 4.4$ kG which gives an undulator parameter of $K = e\bar{B}\lambda_0/2\sqrt{2}\pi mc^2 \approx 1.76$ where the rms field is $\bar{B} = B/\sqrt{2}$. The matched electron beam size is $r_e = (\varepsilon_n\lambda_0/\sqrt{2}\pi K)^{1/2} \approx 0.03$ cm, which minimizes the effect of emittance on beam quality by equalizing the contributions from the radial and angular spreads. The number of betatron oscillations along the undulator length is only $NK/\gamma \approx 0.1$, because of the large Lorentz factor.

The resonant optical wavelength is $\lambda = \lambda_0(1+K^2)/2\gamma^2 \approx 2000$ Å. Because of the short operating wavelength, the small optical mode waist, $W_0 = \sqrt{Z_0\lambda/\pi} \approx 0.03$ cm, is approximately equal to the electron beam radius. Gain is reduced because electrons near the edges of the beam see weak optical fields for bunching.

The electron beam density is $\rho \approx 7\times10^{12}$ cm^{-3} giving a dimensionless current density of $j = 8N[\pi eKL]^2\rho/\gamma^3 mc^2 = 2.7$. There are two correction factors which can be included in j to account for other effects. The filling factor $F = (r_e/W_0)^2/(1+L^2/12Z_0^2)$ accounts for the relative size between the electron beam and the optical mode as it diffracts along the length of the undulator. Because $r_e \approx W_0$, then, for Rayleigh length $Z_0 = L/2$ the filling factor is large. The Bessel function factors, $JJ = J_0(\xi)-J_1(\xi)$, where $\xi = K^2/2(1+K^2)$, expresses the reduced coupling caused by fast periodic z-motion in each undulator period. If $\xi \approx \Delta z/\lambda$ bunching is reduced, and thus, gain is reduced [16]. The theoretical single-mode gain is $G = 0.135j(JJ)^2F \approx 33\%$, but does not include the effects of self-consistent gain, beam quality, beam size, or optical diffraction. [16]

A self-consistent gain calculation includes the changing amplitude and phase of the optical field as the field grows. The field causes bunching of the electrons and the bunching of the electrons leads to a greater increase of the field. When the FEL interaction is calculated self-consistently using the integral equation [16], the gain increases to $G \approx 36\%$. The length of the electron micropulse is $l_e = 0.015$ cm and is 15 slippage distances in length. When the electron pulse length is comparable to the slippage distance each part of the optical pulse will experience gain proportional to the local density of the electron pulse. The resulting effects are known as short-pulse effects [16]. Because the electron pulse length is much larger than the slippage distance, there are no short pulse effects as is typical of short wavelength FELs.

The electron phase velocity is defined as $\nu = L[(k+k_0)\beta_z-k] \approx 4\pi N\Delta\gamma/\gamma$, and measures the degree of resonance between the electron beam, the undulator, and the optical field. An electron beam energy spread causes a spread in phase velocities, $\sigma_G = 4\pi N\Delta\gamma/\gamma \approx 1.3$ with $\Delta\gamma/\gamma = 0.002$ for the CEBAF UV FEL.

The angular and radial spreads of the matched electron beam give equal, but small, contributions to the phase velocity distribution of $\sigma_\theta = 0.3$. When σ_θ or $\sigma_G \approx \pi$, the electron beam is randomly spread over half of an optical wavelength during a pass through the undulator making bunching difficult and decreasing FEL gain. In the CEBAF UV case, the energy spread, with $\sigma_G = 1.3$ distributed in a Gaussian random spread, causes the self-consistent gain calculated with the integral equation [16] to decrease from 36% to $G = 27\%$. The effect of emittance is negligible.

C. OPTIMIZING THE CEBAF UV FEL DESIGN

In order to maximize gain with the basic CEBAF UV FEL design, the effects of dimensionless Rayleigh length, z_0, mode waist position, τ_w, and initial phase velocity, ν_0, on the peak gain was examined. In the FEL interaction, the phase velocity and optical wavelength are not fixed and are free to evolve. Spontaneous emission begins on resonance at $\nu_0 = 0$ and gain grows as ν_0 shifts to satisfy the resonance condition. A gain spectrum is obtained by calculating the gain over a wide range of phase velocities with a self-consistent numerical simulation. The peak gain can then be selected from the gain spectrum. Gain spectra, $G(\nu_0)$, were calculated over a large range of z_0 and τ_w to determine their optimum values and the corresponding optimum gain. The gain spectrum is determined by self-consistent numerical simulations which include the effects of diffraction, beam size and beam quality. When the effects of optical diffraction are included in the FEL interaction, the phase velocity for maximum gain is altered by the Rayleigh length [21]. In the CEBAF UV FEL,

the large electron beam size causes an additional change in the phase velocity. A detailed examination of the effects of electron beam size and diffraction is presented in Chapters V and VI.

As inputs to the numerical solution for the gain spectrum, dimensionless parameters which correspond to the CEBAF UV FEL parameters are used. The peak current density is $j = 2.7$ at the center of the beam, the electron beam radius is $\sigma_e = r_e\sqrt{\pi/L\lambda} = 0.78$ with a parabolic shape, and energy spread is described by $\sigma_G = 1.3$ distributed as a Gaussian. The initially weak optical field is $a_0 = 1$ with dimensionless optical mode radius, $w^2(\tau) = 1+(\tau-\tau_w)^2/z_0^2$, where $\tau = ct/L$ is the dimensionless time along the undulator and τ_w is the position of the optical mode waist along the undulator. The dimensionless Rayleigh length is $z_0 = \pi W_0^2 / L\lambda = Z_0/L$. The transverse dimensionless variables, r and $w(\tau)$, are both normalized to $\sqrt{L\lambda/\pi}$.

For a Gaussian optical mode, a Rayleigh length of $z_0 = 1/\sqrt{12}$ minimizes the optical mode volume averaged over the length of the undulator [16]. For a low-gain FEL with a filament electron beam, the value $z_0 = 1/\sqrt{12} \approx 0.3$ should optimize the gain. An electron positioned at the optical mode waist is at $r = w_0 = \sqrt{z_0}$. Figure 4-1 shows the graph of gain versus Rayleigh length over a large range of values. The initial sharp increase in gain results from the fact that as the Rayleigh length increases the optical mode expands so that more of the electrons are able to participate in the gain process. The nominal value of $z_0 = 1/\sqrt{12}$, which minimized optical mode volume, is not optimum for the CEBAF UV FEL because of the large electron beam size. A larger value of $z_0 = 0.5$ increases the optical mode waist so that more electrons participate in the bunching process. When the optical mode radius and electron beam radius

are approximately equal, the curve in Figure 4-1 begins to flatten and peaks at the value $z_0 = 0.5$. As z_0 continues to increase and expand the optical mode size, less of the optical mode sees electrons and gain is slowly reduced.

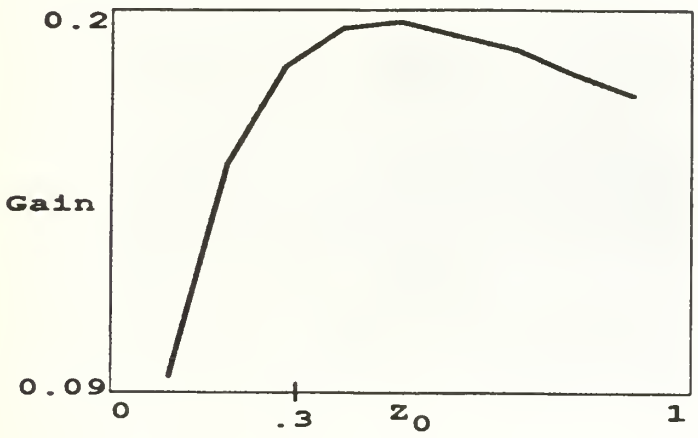

Figure 4-1: Gain versus Rayleigh length for the CEBAF UV FEL parameters. Gain peaks at $z_0 \approx 0.5$.

Figure 4-2 is the graph of gain versus optical mode waist position, τ_w, with the CEBAF UV FEL parameters and $z_0 = 0.5$, as determined above. The curve is symmetric about its peak value of $\tau_w = 0.45$. If the optical mode were positioned at the beginning of the undulator, light would quickly diffract and reduce the mode amplitude near the end of the undulator. The low optical amplitude would reduce coupling with the bunched electrons. If the optical mode waist were positioned near the end of the undulator, the larger optical mode in the first half of the undulator would provide less optical amplitude to bunch the electrons. In this case, the optimum mode waist position is to focus the light just prior to the center of the undulator to increase the electron bunching. Toward the end of the undulator, mode distortion helps to keep the optical mode focused toward the electron beam and gain is maximized.

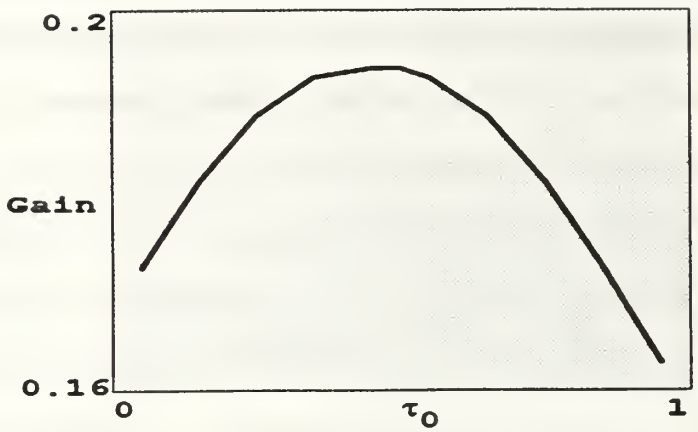

Figure 4-2: Gain versus optical mode waist position for CEBAF UV FEL parameters. Gain peaks at $\tau_w \approx 0.45$.

Figure 4-3 shows the gain spectrum, $G(\nu_0)$, for the CEBAF UV FEL determined by self-consistent numerical simulation including diffraction, beam size, and beam quality. The optimum resonator design described by a Rayleigh length of $z_0 = 0.5$, and waist position $\tau_w = 0.45$ is used in Figure 4-3. The maximum gain obtained is $G \approx 20\%$ at a phase velocity of $\nu_0 \approx 4.3$.

Figure 4-4 shows the result of a numerical simulation of the CEBAF UV FEL radiation wavefront as τ goes from 0 to 1 along the $N = 50$ period undulator. The optical wavefront has an initially weak field amplitude $a_0 = 1$ at the mode center with phase curvature that gives Rayleigh length $z_0 = 0.5$ focused at $\tau_w = 0.45$ in the absence of the FEL interaction. The electron beam is parabolic in shape with radius $\sigma_\theta = 0.78$, phase velocity $\nu_0 = 4.3$, current density $j = 2.7$ at the center of the beam, and energy spread $\sigma_G = 1.3$.

The evolution of the optical mode amplitude, $|a(x,\tau)|$ (upper-left), is shown as an intensity/contour plot with the x and y axes scaled to $\sqrt{L\lambda/\pi}$. The maximum field is white and zero field is black with one contour. The greyscale

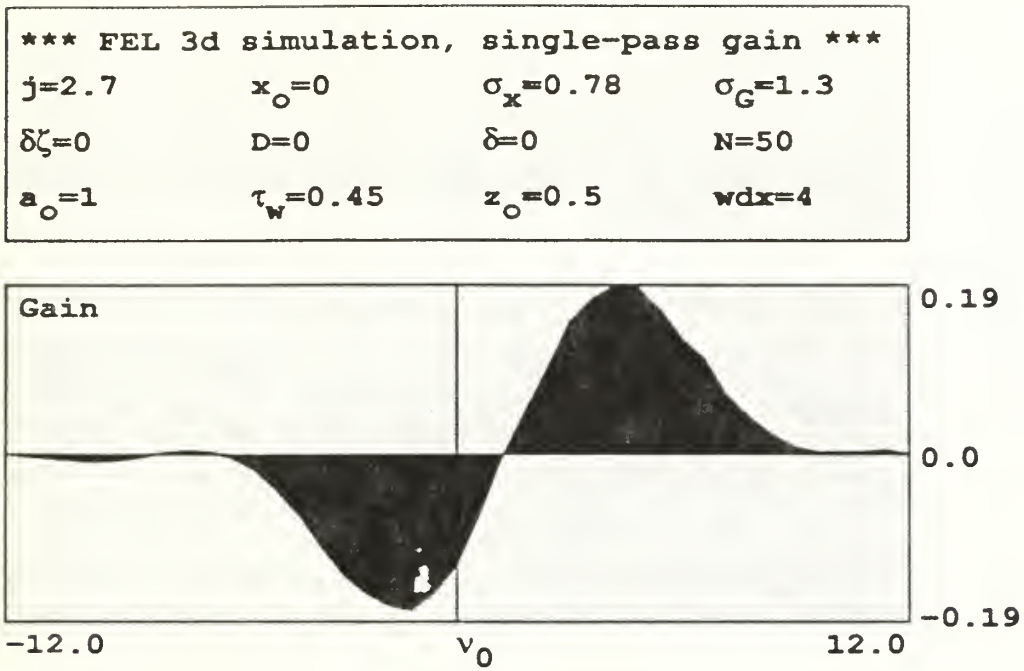

Figure 4-3: Gain spectrum for the CEBAF UV FEL using optimized parameters. Peak gain occurs at $\nu_0 = 4.2$.

for each plot is shown at the right. The mode focuses just before the middle of the undulator, $\tau = \tau_w = 0.45$. At the end of the undulator the mode expands significantly in the absence of the FEL interaction, but in the plot of $|a(x,y)|$ (upper-center) the mode is slightly focused in toward the electron beam. The evolution plot of the bunching current, $\sigma(x,\tau) \propto j(r)\langle\cos(\zeta+\phi)\rangle$ (middle-left), shows the electron bunching developing along the length of the undulator. The final bunching $\sigma(x,y)$ (middle-center) is smaller than the optical mode because bunching is maximum where both the light intensity and beam current are maximum. This tends to slightly focus the wavefront even though the laser and electron beams are about the same size. The electron phase velocity distribution, $f(\nu,\tau)$ (lower-left), shows only small distortion in weak optical fields. The final electron phase-space distribution in (ζ,ν) (lower-center) shows the

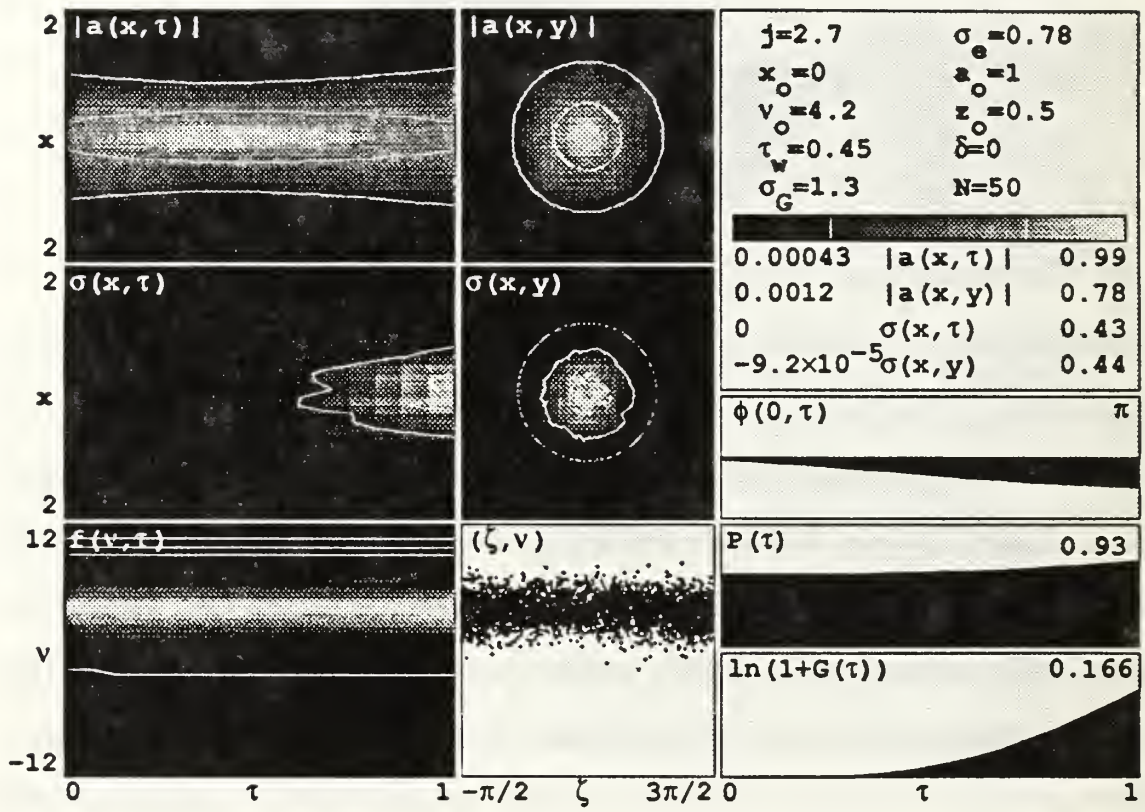

Figure 4-4: Numerical simulation of the CEBAF UV FEL radiation wavefront in weak fields.

slight electron bunching at the end of the undulator in the weak optical field. Note that some electrons remain at the initial phase velocity, $v_0 = 4.3$, because they are at the edge of the optical mode and see only low intensity light. The plot of the phase evolution at the center of the mode, $\phi(0,\tau)$ (on the right), shows the approximate linear decrease in phase $\propto -\tau/z_0$ described in (2). The power evolution, $P(\tau)$, and gain evolution, $\ln(1+G(\tau))$ (on the right), show the development of the final gain, $G = 20\%$. There is little gain in the beginning of the undulator while bunching develops.

Figure 4-5 shows the result of a wavefront simulation for the same FEL as in Figure 4-4, but with an initially strong optical field amplitude of $a_0 = 40$. The phase velocity is increased to $v_0 = 6$ for more optimal gain in strong fields [16]. The gain evolution, $\ln(1+G(\tau))$, shows the gain developing early along the undulator due to the larger field strength. The same effect is seen in the plot of the bunching current $\sigma(x,\tau)$. The electron phase velocity distribution, $f(v,\tau)$, shows the wider spread in strong fields, while the phase-space plot, (ζ,v), shows overbunching. The bunching current evolution $\sigma(x,\tau)$ and final bunching distribution $\sigma(x,y)$ show a "hole" in the middle of the beam resulting from the overbunching in strong fields. Here, the electrons are actually taking energy back from the center of the optical mode at saturation. The small angular spread from the high-quality matched electron beam, $\bar{\theta} = \varepsilon/r_e \approx 5\times10^{-5}$, does not allow mixing of the inner and outer parts of the beam. The transverse drift of an electron is only one-tenth of the beam radius over the last fifth of the undulator length. As the optical mode and electron distribution continue to evolve over many passes in stronger fields, the trapped-particle instability may occur and cause a hole to develop at the center of the optical mode.

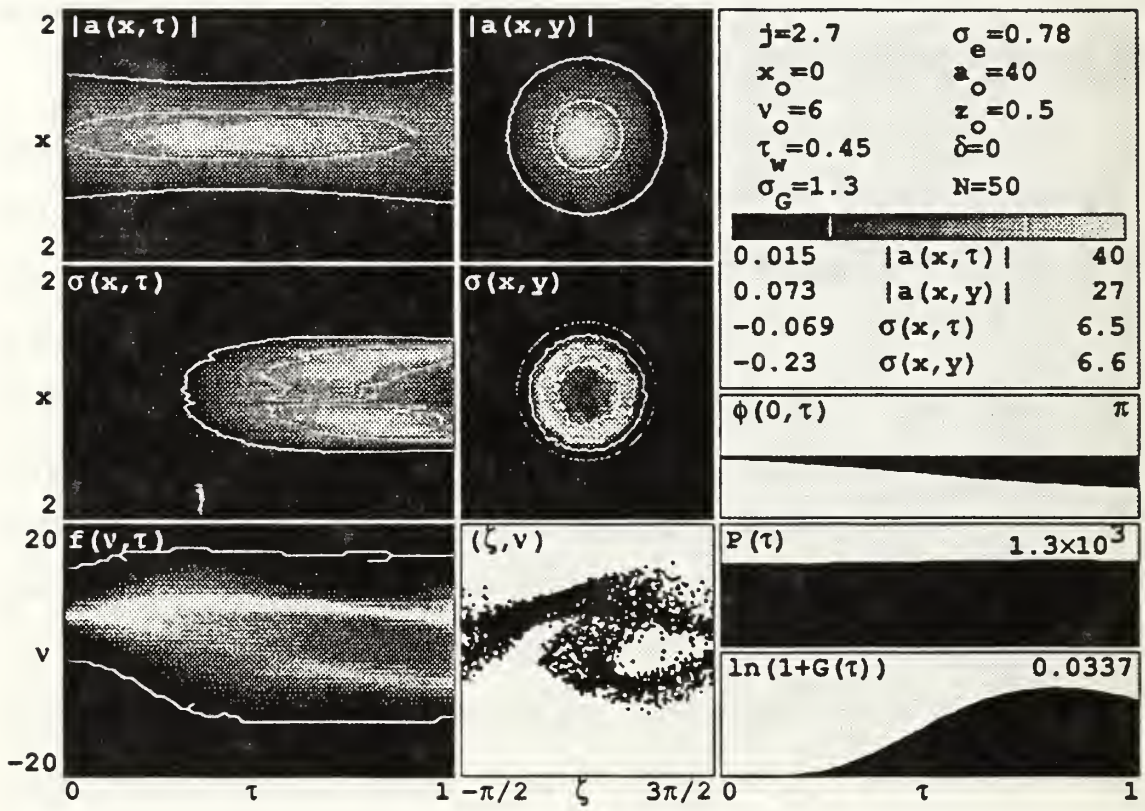

Figure 4-5: Numerical simulation of the CEBAF UV FEL radiation wavefront in strong fields.

D. ALTERNATIVE DESIGNS FOR THE CEBAF UV FEL

The basic CEBAF UV FEL design appears attractive because of its good performance at short wavelengths using the conventional FEL interaction. The $N = 50$ period undulator has moderate gain without serious degradation due to beam quality. The CEBAF continuous beam of micropulses must only be slightly above the resonator loss to achieve saturation in strong optical fields. At normal incidence from $\lambda \approx 1000 \rightarrow 2000$ Å, clean Al in ultra-high vacuum has only 4% loss, and dielectric multilayers of MgF_2 on Al has only 2% loss [22]. The following three design modifications may improve gain, but with some added risk depending on the details of increased sensitivity to the electron beam quality. An increased sensitivity to beam quality may have greater than anticipated effect on gain because, until the accelerator is completed and begins operation, the true electron beam quality is unknown.

Longer Undulator: When an FEL is not seriously degraded by beam quality, the design may benefit by increasing the undulator length L. As the UV undulator length is increased to $L = 600$ cm with $N = 100$ periods, the optimum Rayleigh length, $Z_0 = L/\sqrt{12}$, can be used because the optical mode waist radius increases $\propto L^{1/2}$. The filling factor is then decreased to a more optimal value of $F \approx 0.5$ with fewer electrons in the tails of the wider Gaussian optical mode. The dimensionless current density, $jF \propto N^3F$, is dramatically increased to $jF \approx 11$ and increases the potential for much higher gain. However, the penalty for a longer undulator is increased sensitivity to beam quality. The increased spreads due to energy spread and emittance are $\sigma_G = 2.5$ and $\sigma_\theta = 0.6$. Assuming the energy spread is distributed as a Gaussian and the emittance is spread in the exponential distribution [16], the UV gain is calculated to be more than 70% for the longer undulator. This is an attractive gain for a FEL oscillator

at shorter wavelengths because mirror losses can be significant. With a longer undulator, it appears than the CEBAF UV FEL could be extended to reach wavelengths shorter than $\lambda = 2000$ Å, but would become sensitive to the unknown shape of the $f(\nu_0)$ distribution.

Smaller Electron Beam: The UV FEL gain is significantly reduced because some of the electrons are in the tails of the optical wavefront. Making the electron beam smaller in the transport system of the accelerator reduces this effect at the expense of an increase in the contribution of angular spread to poor beam quality in σ_θ. If the radius of the beam at the waist is reduced to $r_e = 0.17$ mm, then the angular spread is increased so that the beam radius roughly doubles its size to $r_e = 0.3$ mm at each end of the undulator. The previously negligible angular spread is now $\sigma_\theta = 1.2$, and has a significant contribution on beam quality roughly equal to the energy spread contribution, $\sigma_G = 1.3$. The net result is favorable and raises the gain to 36% including diffraction, energy spread, and angular spread. As with the longer undulator, the smaller electron beam would give more gain, but would again become more sensitive to the unknown shape of the $f(\nu_0)$ distribution.

FEL Klystron: The FEL klystron increases gain in weak optical fields at the expense of low-power saturation and increased sensitivity to beam quality [16]. The FEL klystron consists of two undulator sections separated by either a drift or a dispersive section. The drift and dispersive mechanisms are the same mathematically, but in practice, it is the dispersive section that gives a substantial increase to the FEL gain for a given interaction length. It is also advantageous that the strength of the dispersive section can be controlled during the experiment. Using the CEBAF UV FEL parameters including energy spread, the strength of the dispersive section was increased to find the

maximum gain. Because of the increased sensitivity to beam quality, no significant increase in gain was obtained over the conventional design. For a stronger klystron the effects of beam quality decreased the gain and countered the benefits of the klystron.

V. FELS WITH LARGE FILLING FACTOR

A. INTRODUCTION

As FEL experiments strive for shorter wavelengths, the size of the optical mode will become comparable to the size of the electron beam and the filling factor will increase. This was seen in the CEBAF UV FEL in Chapter IV. The theoretical single-mode gain is $G = 0.135jF$, but does not include the effects of self-consistent gain, beam quality, beam size or optical mode diffraction. According to the theoretical single-mode gain, as F increases, G increases. In reality, as the optical mode size approaches the electron beam size, fewer of the electrons are able to effectively participate in the bunching process. The result is that gain is reduced. Additionally, electrons across the electron distribution within the beam contribute to a larger phase shift.

Figure 5-1 shows the size relation between a parabolic electron distribution and a Gaussian optical mode for a small, medium, and large optical mode. In the figure at the left, the optical mode is large and the electron beam is completely contained in the optical mode where the optical mode amplitude is large. All of the electrons will participate in the gain process. In the center figure, the optical mode and electron beam are of roughly equal size. Some of the electrons at the edge of the beam exist where the optical amplitude is small. These few electrons will not contribute significantly to the gain process. In the figure at the right, the electron beam is larger than the optical mode. Here, many of the electrons see a small optical amplitude and will not participate in the gain process.

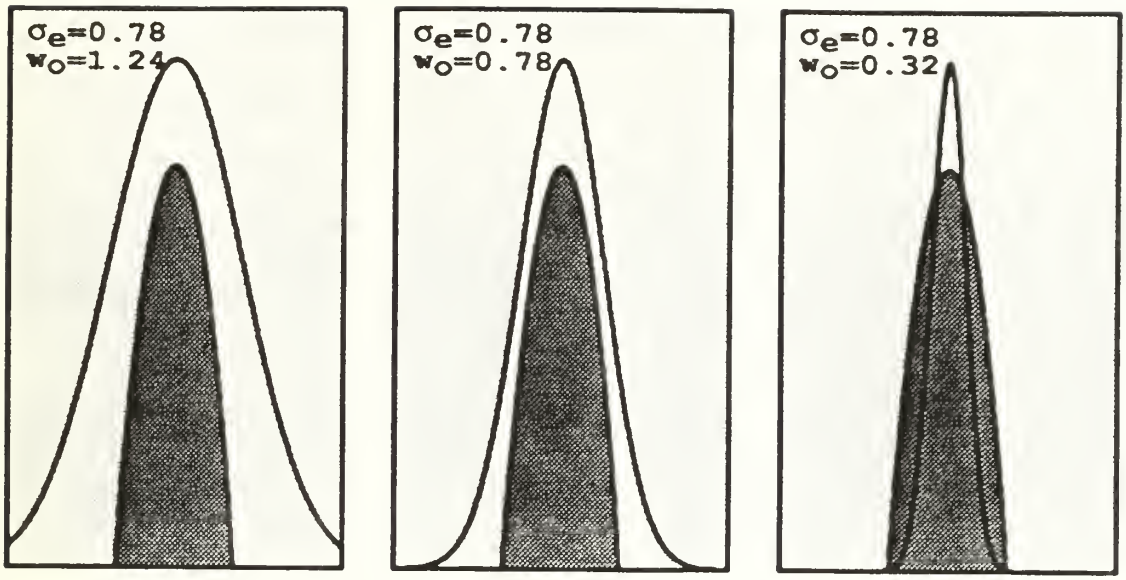

Figure 5-1: Comparison of a parabolic electron distribution (dark) to a large, medium and small Gaussian optical mode (light).

B. THE PHASE VELOCITY RESONANCE SHIFT

1. The Resonant Phase Velocity

The maximum of the FEL gain spectrum is shifted by optical diffraction when z_0 is finite [23]. As in the CEBAF UV FEL, a large electron beam size causes an additional change in the phase velocity.

To estimate the shift in resonance, consider the free Gaussian optical mode [16] as an approximate for the optical field when the gain is low. The Gaussian optical field is

$$a_G(r,\tau) = \frac{a_0}{w(\tau)} \exp\left[\frac{-r^2}{w^2(\tau) z_0}\right] \exp[i\phi_G(\tau)] \quad , \qquad 5\text{-}1$$

with phase

$$\phi_G(\tau) = -\tan^{-1}\left[\frac{(\tau - \tau_w)}{z_0}\right] + \frac{r^2(\tau - \tau_w)}{z_0^2 + (\tau - \tau_w)^2} \quad , \qquad 5\text{-}2$$

where r is the dimensionless distance off axis, $w^2(\tau) = 1+(\tau-\tau_w)^2/z_0^2$ is the dimensionless optical mode radius, z_0 is the dimensionless Rayleigh length, τ is the dimensionless time along the undulator, τ_w is the position of the optical mode waist along the undulator, and a_0 is the dimensionless optical amplitude at $r = 0$. From equation 5-1, a Rayleigh length of $z_0 = 1/\sqrt{12}$ will minimize the optical mode volume averaged over the length of the undulator.

The electron pendulum equation [16, 21] describes the bunching of electrons in the presence of the optical field in equations 5-1. If the Rayleigh length is large, $z_0 \rightarrow \infty$, equation 5-1 becomes a plane wave so that the optical mode is much wider than the electron beam, and the phase shift in equation 5-2 becomes negligible. When the Rayleigh length is finite and the electron beam is wide, the optical phase shift can be significant and can also influence the FEL interaction. To evaluate the effect of a finite Rayleigh length, equations 5-1 and 5-2 are substituted into the pendulum equation $\overset{\circ\circ}{\zeta} = |a_G(\tau)|\cos[\zeta+\phi_G(\tau)]$ where $\zeta = (k+k_0)z(t)-\omega t$ is the electron phase derived in Chapter III. Expanding in powers of z_0^{-1} to simplify the expression, to second order in z_0^{-1}, $\phi_G(\tau) \approx -(\tau-\tau_w)/z_0 + r^2(\tau-\tau_w)^2/z_0^2 + O(z_0^{-3}) + \cdots$, the pendulum equation for an electron in a Gaussian optical mode with weak optical field strength, $a_0 < \pi$, becomes

$$\overset{\circ\circ}{\zeta} = a_0\left[1-\frac{r^2}{z_0}-\frac{(\tau-\tau_w)^2}{2z_0^2}\right]\cos\left[\zeta_0+\left[1-\frac{r^2}{z_0}\right]\frac{\tau_w}{z_0}+\Omega\tau\right] \quad , \qquad 5\text{-}3$$

where the electron phase is $\zeta_0 = (k+k_0)z_0-\omega t$ at position z and time t, $k = 2\pi/\lambda$ is

the optical wavenumber, $k_0 = 2\pi/\lambda_0$ is the undulator wavenumber, and ζ_0 is the initial electron phase. The last term in equation 5-3 is

$$\Omega = v_0 - \frac{1}{z_0} + \frac{r^2}{z_0^2} \quad , \qquad 5\text{-}4$$

where v_0 is the initial phase velocity.

The amplitude of the field in equation 5-3 increases and decreases in time, τ, along the undulator with maximum amplitude at the mode waist position $\tau = \tau_w$. When the electrons are off-axis, the field amplitude is weaker. The electron phase is shifted by a term proportional to τ_w, but this shift is inconsequential because the electrons are randomly spread in ζ_0. The electron phase velocity is proportional to the evolving time τ, and is also shifted by the finite Rayleigh length and the radial position r.

Equation 5-4 can be identified as the new phase velocity which has important consequences because maximum FEL gain occurs when $\Omega = 2.6$ [16]. For an FEL with a filament electron beam ($r \approx 0$ for all electrons), the maximum gain occurs at $v_0^{max} \approx 2.6 + 1/z_0$. If $z_0 = 1/\sqrt{12}$, the maximum gain occurs at $v_0 \approx 6$ instead of $v_0 \approx 2.6$ for plane waves with $z_0 \rightarrow \infty$. Because the gain spectrum bandwidth is $\Delta v_0 \approx \pi$, this is a significant shift [21].

If the electron beam is not a filament, the effect of the electrons injected off-axis must be accounted for by finding the weighted average of the square of the off-axis injection distance over some normalized electron distribution function $f(r)$. The distribution function is normalized such that $\int f(r)\, r dr d\theta = 1$. The resonant phase velocity in equation 5-4 becomes

$$v_0^{max} = 2.6 + \frac{1}{z_0}\left[1 - \frac{\langle r^2 \rangle}{z_0}\right] \quad , \qquad 5\text{-}5$$

where, in general, the average of the off-axis injection distance square is $\langle r^2 \rangle = \int_0^{2\pi} \int_0^R r^2 f(r)\, r dr d\theta$, where R is the maximum radius of the distribution.

2. The Parabolic Electron Distribution

If the electron beam cross-section has a parabolic shape so that

$$f(r) = \frac{1}{\pi\sigma_e^2}\left[1 - \frac{r^2}{2\sigma_e^2}\right] \quad , \qquad 5\text{-}6$$

with normalized width $\sigma_e = r_e(\pi/L\lambda)^{1/2}$ and maximum radius $R = \sqrt{2}\sigma_e$, then the average square radius is

$$\langle r^2 \rangle = \frac{1}{\sqrt{2}\sigma_e^2}\int_0^{2\pi}\int_0^{\sqrt{2}\sigma_e} r^2 \left[1 - \frac{r^2}{2\sigma_e^2}\right] r dr d\theta = \frac{2}{3}\,\sigma_e^2 \quad . \qquad 5\text{-}7$$

Substituting equation 5-7 into equation 5-5, the resonant phase velocity for a parabolic electron beam of width σ_e is

$$v_0^{max} = 2.6 + \frac{1}{z_0} - \frac{2\sigma_e^2}{3z_0^2} \quad . \qquad 5\text{-}8$$

Simulations of the CEBAF UV FEL in Chapter IV showed that peak gain occurred at $z_0 = 0.45$ and $v_0 = 4.3$. Equation 5-8 with $z_0 = 0.5$ and $\sigma_e = 0.78$ predicts that maximum gain will occur at $v_0 = 3.0$, neglecting the effects of beam quality. For a Gaussian distribution, the phase velocity for peak gain is shifted by about $\sigma_G = 4\pi N \Delta\gamma/\gamma$ [16]. For the CEBAF case, $\sigma_G = 1.3$. Including the effects of diffraction, beam size, and beam quality, the predicted value of $v_0^{max} = 2.6 + 2 - 1.6 + 1.3 = 4.3$ in close agreement with the simulations.

Figure 5-2 displays a graph of v_0^{max} versus Rayleigh length for an FEL with low gain ($j = 0.1$) and a filament electron beam ($\sigma_e = 0.1$). The dark line is a plot of equation 5-8, and the grey line is a plot of v_0^{max} including diffraction

only. The "X"s are data points taken from three-dimensional self-consistent simulations. The graph shows that for a small electron beam equation 5-8 is valid over a large range of Rayleigh lengths. The data points correspond closely with both plotted lines because the correction factor for the electron beam size, $-2\sigma_e^2/z_0^2$, is small. The correction factor for the beam size is small as long as σ_e is small and z_0 is large. For small electron beams, equation 5-8 is valid for $z_0 > 0.2$. Even where equation 5-8 is not an accurate estimate of the resonant phase velocity, the actual phase velocity tends toward the value predicted by equation 5-8.

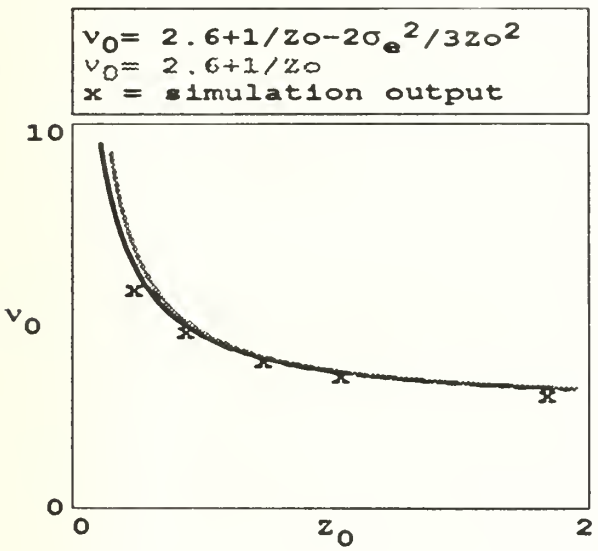

Figure 5-2: Optimum phase velocity versus Rayleigh length for a small parabolic electron beam. Equation 5-8 is valid for $z_0 > 0.2$.

Figure 5-3 displays a graph of v_0^{max} versus Rayleigh length for an FEL with low gain ($j = 0.1$) and a large electron beam ($\sigma_e = 0.7$). Again the grey line is a plot of v_0^{max} including diffraction only. v_0^{max} including the effects of diffraction and beam size is plotted as a dark line, and the "X"s indicate data points taken from simulations. This graph shows that for a large electron beam the

correction factor is larger and diverges from the actual v_0^{max} at a larger Rayleigh length. The correction factor in equation 5-8 is larger so that equation 5-8 is valid over a smaller range of Rayleigh lengths. The difference can be attributed to the finite value of z_0 in the expansion for equation 5-3.

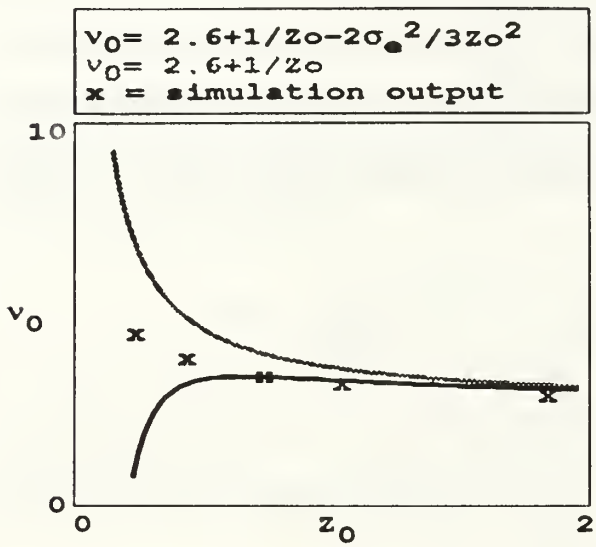

Figure 5-3: Optimum phase velocity versus Rayleigh length for a large parabolic electron beam. Equation 5-8 is valid for $z_0 > 0.5$.

3. The Gaussian Electron Distribution

Assuming a Gaussian distribution to the electron beam profile, then

$$f(r) = \frac{1}{2\pi\sigma_\theta^2} e^{-r^2/2\sigma_\theta^2} \quad , \qquad 5\text{-}9$$

describes the electron distribution. The average electron squared radius is of

$$\langle r^2 \rangle = \frac{1}{2\pi\sigma_\theta^2} \int_0^{2\pi} \int_0^{\infty} r^2 e^{-r^2/2\sigma_\theta^2} r dr d\theta = 2\sigma_\theta^2 \quad . \qquad 5\text{-}10$$

Here the radius of the Gaussian distribution is taken to be infinite in order to complete the integration in equation 5-10. However, when performing

simulations using a Gaussian electron distribution a cutoff radius must be assumed. This will increase the errors of the final solution. Equation 5-10 is substituted into equation 5-3 to find the phase velocity for maximum gain including beam quality is

$$v_0^{max} = 2.6 + \frac{1}{z_0} - 2\,\frac{\sigma_e^2}{z_0^2} \quad . \qquad 5\text{-}11$$

Overall, the equation for the resonant phase velocity including beam size is much less accurate for the Gaussian beam than for the parabolic beam. The reason is that many more of the electrons lie farther from the beam center. These electrons lead to a large value for the average square radius, but because the optical field is very weak at the edges, they contribute little to the FEL gain and phase shift. The principle that a wide electron beam will lead to a shift in resonant phase velocity is still validated by this analysis.

C. GAIN DEGRADATION WITH LARGE ELECTRON BEAMS

Figure 5-4 shows the decrease in gain $G(\sigma_e)/G_0$ as the electron beam increases beyond the optical mode waist [20]. The gain is determined numerically for a parabolic current density, and is compared to the theoretical single-mode gain $G_0 = 0.135jF$ for a filament beam, while σ_e is compared to w_0. The Rayleigh length is $z_0 = 0.5$ and waist position is $\tau_w = 0.5$ with phase velocity for near maximum gain at $v_0 = 4$ in a weak optical field $a_0 = 1$. The current density is taken to be $jF = 1.0$. At each value of σ_e/w_0 the filling factor changes, and the peak current density j increases keeping jF fixed. At $\sigma_e/w_0 \approx 0.8$, the actual gain, $G(\sigma_e)$, and filament gain, G_0, are equal. For larger beams, the gain decreases significantly below the filament gain.

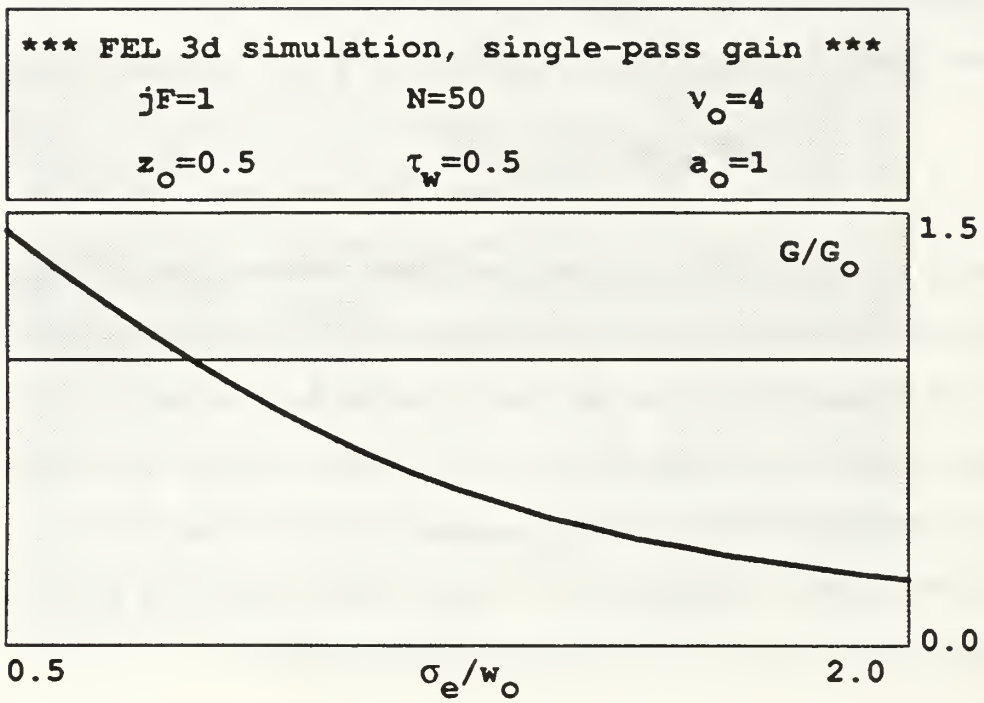

Figure 5-4: Relative Gain versus Relative Beam/Mode size for low gain FEL.

For values of $jF \leq 1$ down to $jF = 0.001$, the curve in Figure 5-3 remains essentially unchanged. For $jF \geq 1$, there is a small upward shift in gain on the left side of the curve at small values of σ_e/w_0. For $jF \geq 10$, the upward shift is more pronounced and is caused by optical mode distortion when the current j becomes large. For $jF \leq 1$, the value of z_0 can be varied from ≈ 0.3 to ≈ 0.7 with no significant change to the curve. The actual value of the current density for the CEBAF UV FEL is $jF = 2.4$ where $j = 2.7$ and $F = 0.9$, so that the curve in Figure 5-4 can be used to describe the gain degradation in that experiment. Figure 5-4 appears to have a wide range of validity, and is useful for experimental design of FELs with large electron beams.

D. DISCUSSION

The resonant phase velocity of an FEL is shifted by diffraction and by a finite electron beam size. By calculating the average off-axis electron injection distance, the new resonant phase velocity can be predicted over a range of Rayleigh ranges and electron beam sizes. The range of z_0 over which equations 5-8 and 5-11 hold is a result of the assumption that $z_0 \gg 1$ in the expansion of the optical mode and the phase of the Gaussian optical mode. Because of this assumption, the analytical solution for v_0^{max} is most accurate when $z_0 > 0.5$. When longer Rayleigh ranges are used, the solutions above can be a sufficiently accurate estimate of the resonant phase velocity. For small electron beams ($\sigma_e < 0.5$), the predicted resonant phase velocity remains accurate to smaller values of z_0. However, if the electron beam is large in comparison to the optical mode size, the solution for the resonant phase velocity at short Reyleigh ranges is less accurate, particularly for Gaussian electron beams. An empirical solution for the phase velocity for a parabolic beam is $v_0^{max} = 2.6+1/z_0-2\sigma_e^2/5z_0^2$. The analogous empirical solution for Gaussian beam is $v_0^{max} = 2.6+1/z_0-\sigma_e^2/z_0^2$. Both of these solutions are much more accurate over a larger range of electron beam sizes and Rayleigh lengths. They may be used to predict the resonant phase velocity for maximum gain in many experiments.

The reduction in gain for an FEL with large filling factor results from the non-participation of electrons which lie near the edges of the electron beam. Figure 5-4 presented in Section C of this chapter, can serve as a kind of "universal" gain curve to provide a simple prediction for FEL gain for experiments with a wide range of dimensionless electron currents and filling factors.

VI. OPTICAL MODE DISTORTION

A. INTRODUCTION

The optical field in an FEL can be thought of as the superposition of the input optical field and the excited optical field, which results from stimulated emission [24]. Assuming that the input optical field is a Gaussian, the field can be observed to focus toward the optical mode waist and then diffract out again away from the axis at a rate inversely proportional to the Rayleigh length. In dimensionless units $w_0 = \sqrt{z_0}$, and the optical mode radius is $w^2 = 1+(\tau-\tau_w)^2/z_0^2$. The "new light" of the excited optical field begins near the electron beam. If the electron beam is much narrower than the optical mode, the excited field has an effective mode waist and Rayleigh length much smaller than the input optical mode and will diffract much more rapidly.

B. THE NUMERICAL SIMULATION

The effects of gain and electron beam size on the excited optical field can be observed through numerical simulations of the FEL interaction by subtracting the input optical field from the total optical field as they develop along the undulator. This chapter examines these effects with a modification of the simulation used to produce the output figures for the CEBAF UV FEL in Chapter IV. The simulation program uses numerical integration of the parabolic wave equation coupled with the electron Lorentz force equation [16]. This numerical simulation accounts for many transverse modes self-consistently and is general enough to include different undulator designs, optical mirror

arrangements and driving currents. The evolution of the optical fields and electron currents are shown as an intensity/contour plot with the x and y axes scaled to $\sqrt{L\lambda/\pi}$. The maximum field is white and the minimum field is black with two constant amplitude contours.

These simulations begin in weak optical fields $a_0 = 1$ with phase curvature that gives Rayleigh length $z_0 = 0.3$ that will focus at $\tau_w = 0.5$ without the FEL interaction. The electron beam will have a parabolic shape with radius, σ_e, phase velocity, $v_0 = 6$, and current density, j, at the center of the beam. For these simulations it is assumed that there is no energy spread or emittance in order to observe the most simple result of the optical mode distortion. Energy spread and emittance can be included when desired.

The simulation follows two independent optical mode evolutions through the undulator. The first is the undistorted optical field developed with $j = 0$. The second is the total optical field developed through the fully self-consistent simulation with j and σ_e equal to some appropriate value. The output of this simulation shows the difference between the total optical field amplitude and the input field amplitude as they develop along the undulator, $\Delta|a(x,\tau)|$, and at the end of the undulator, $\Delta|a(x,y)|$. Because this is a difference of amplitudes, it may display negative values. These negative values occur where the input optical field and the excited optical field destructively interfere so that the total optical field is less than the input optical field. The difference in phase between the total optical field and the input optical field along the axis is plotted as $\Delta\phi(\tau)$.

C. THE INPUT OPTICAL FIELD

Figure 6-1 shows a Gaussian optical mode in an FEL undulator. The dimensionless current density, j, is zero so there is no gain, and the power (lower-right) remains constant. Because there is no excited field, the input optical mode remains undistorted throughout the undulator. In the evolution of the optical field amplitude through the undulator, $|a(x,\tau)|$ (upper-left), the optical mode focuses at the optical mode waist, τ_w, and later begins to spread. Because the dimensionless Rayleigh length is $z_0 = 0.3$, the optical mode area doubles at $\Delta\tau = \pm 0.3$ on either side of τ_w. The input optical mode amplitude at the end of the undulator, $|a(x,y)|$ (upper-middle), remains in a Gaussian distribution. The blocks which describe the electrons, $\sigma(x,\tau)$ and $\sigma(x,y)$, and the phase velocity evolution, $f(\nu,\tau)$, are blank because there are no electrons used in the simulation.

D. THE EFFECT OF BEAM SIZE ON MODE DISTORTION

The waist of the excited optical field, w_e, is roughly equal to the electron beam size [24], so that the Rayleigh length of the new light can be much shorter than that of the input optical mode. Therefore, the Rayleigh length for the new light is determined by $z_e \approx \sigma_e^2$. If the input optical mode is much larger than the electron beam then $z_0 \gg z_e$, and the excited optical field will diffract much more quickly than the input optical field. To show the effect of the electron beam size on the excited mode, several simulations were run where the product $j\sigma_e^2$ is held constant in order to maintain the same single mode gain. Figures 6-2 through 6-5 show four examples where $j\sigma_e^2 = 0.1$.

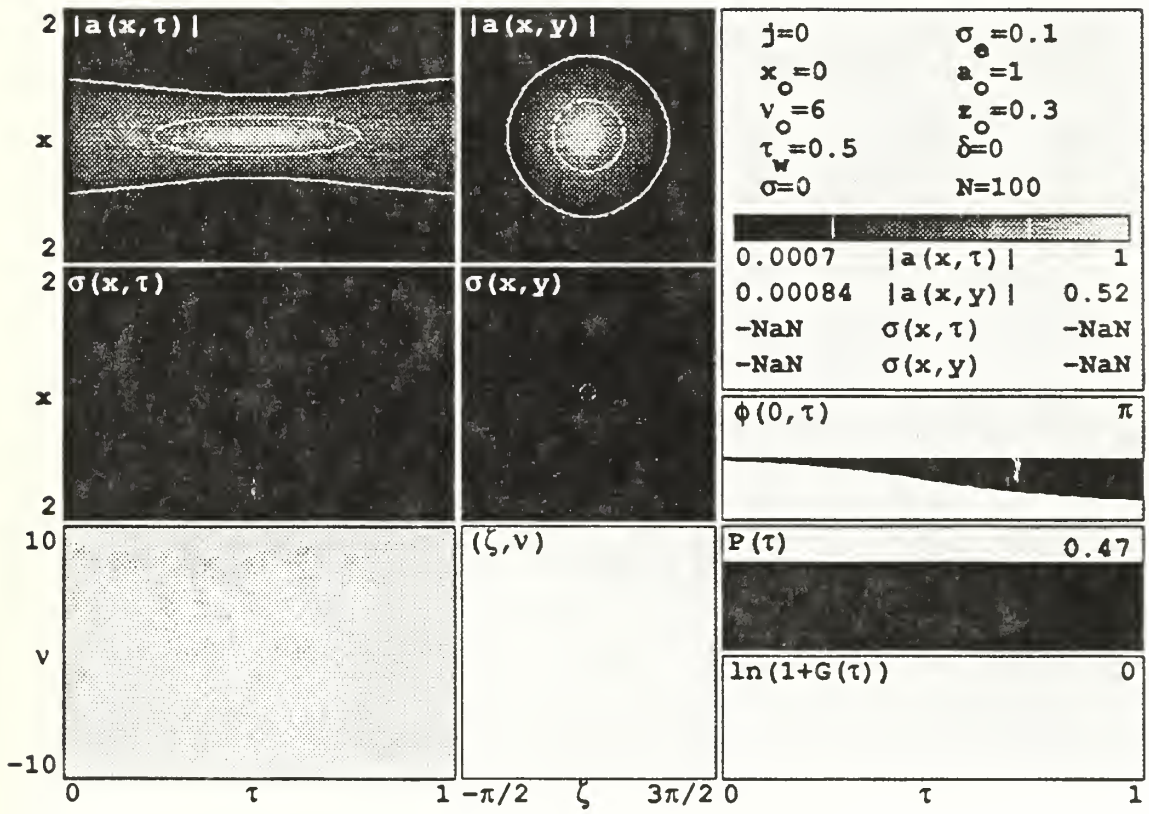

Figure 6-1: Free Gaussian optical mode in an FEL undulator.

In Figure 6-2, the wide electron beam results in a wide excited mode, $\Delta|a(x,\tau)|$. The excited mode remains close to the electron beam axis. The difference in the phase between the total optical field and the input optical field, $\Delta\phi(0,\tau)$, is very small. In Figure 6-3 the excited optical field is initially more narrow, but diffracts to a larger area at the end of the undulator. The area just outside the second contour corresponds to nearly zero amplitude. Farther outside the second contour there is destructive interference between the input and excited modes so that the resulting difference in amplitudes is negative. The phase difference between the two modes has grown, but is still small. Figure 6-4 continues the trend as the waist continues to narrow causing rapid diffraction with a small phase difference.

In Figure 6-5 there is a major difference. The overall trend of the narrower electron beam rapidly diffracting away from the undulator axis is continuing, but a hole has developed at the center of the excited optical field near the end of the undulator. The size of the hole roughly corresponds to the size of the electron beam. The evolution of the average electron driving current, $\sigma(x,\tau)$ shows that the electrons are bunched at the end of the undulator. The gain evolution, $\ln(1+G(\tau))$, shows a maximum at the end of the undulator. The excited field at the end of the undulator in Figure 6-5 forms a "doughnut" around the undulator axis.

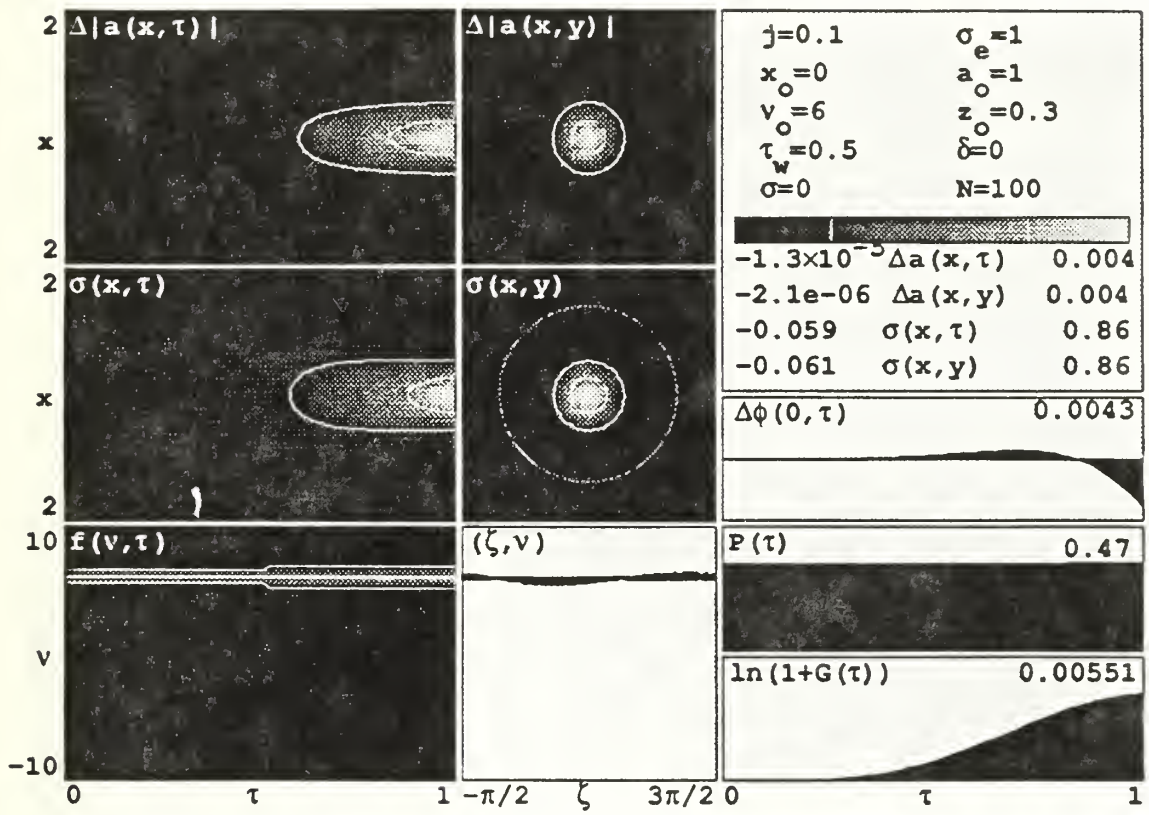

Figure 6-2: The excited optical field of a low gain FEL with a wide electron beam.

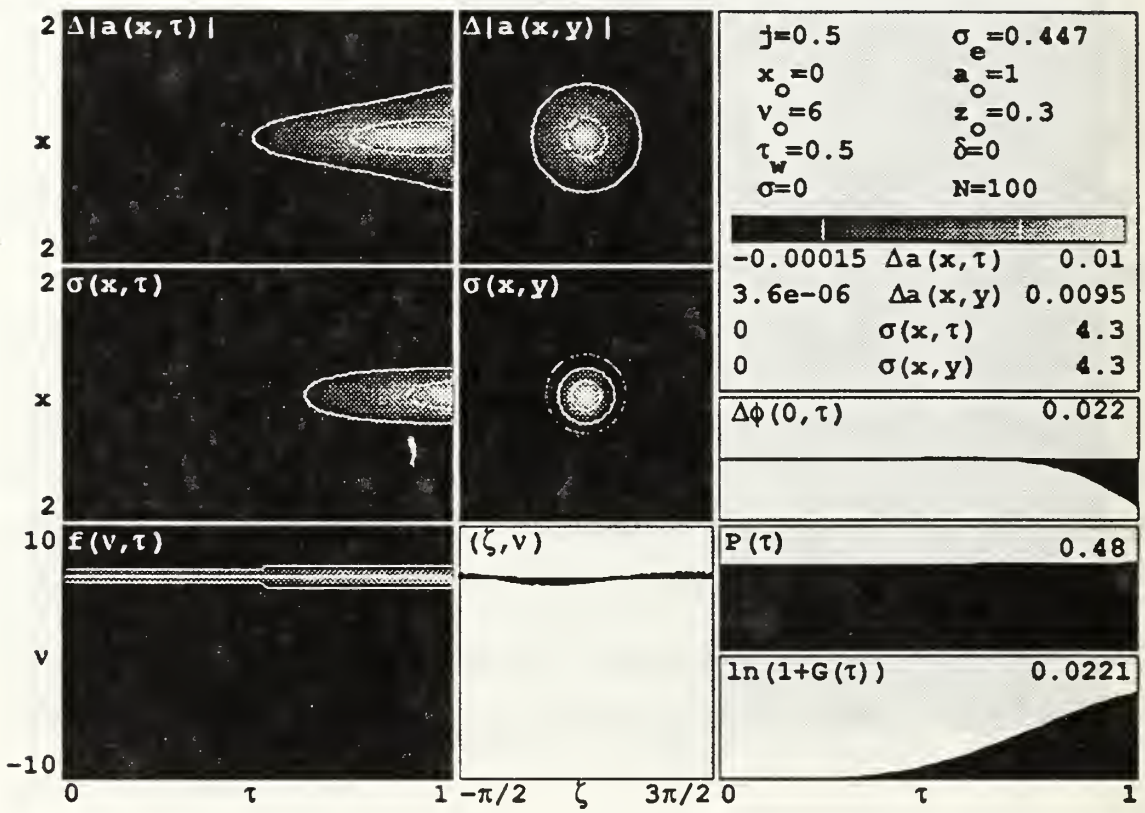

Figure 6-3: The excited optical field of a low gain FEL with optical mode slightly larger than the electron beam.

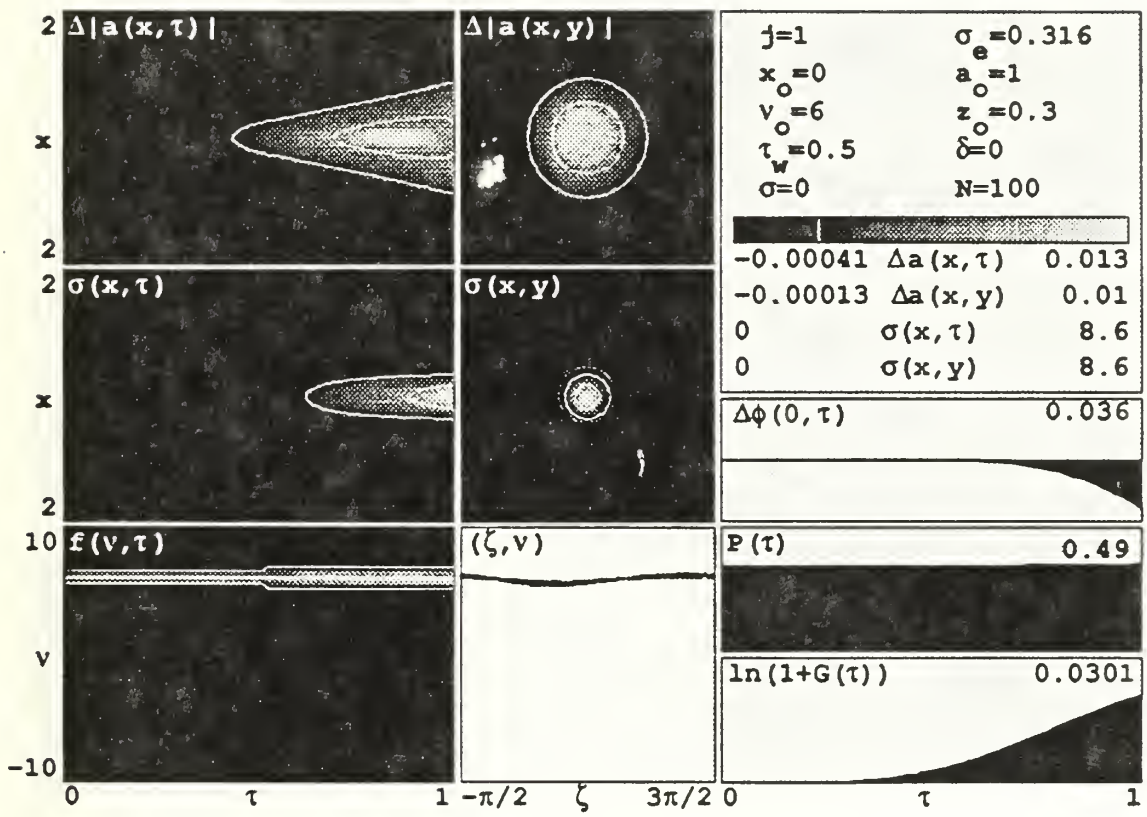

Figure 6-4: The excited optical field of a low gain FEL with optical mode larger than the electron beam.

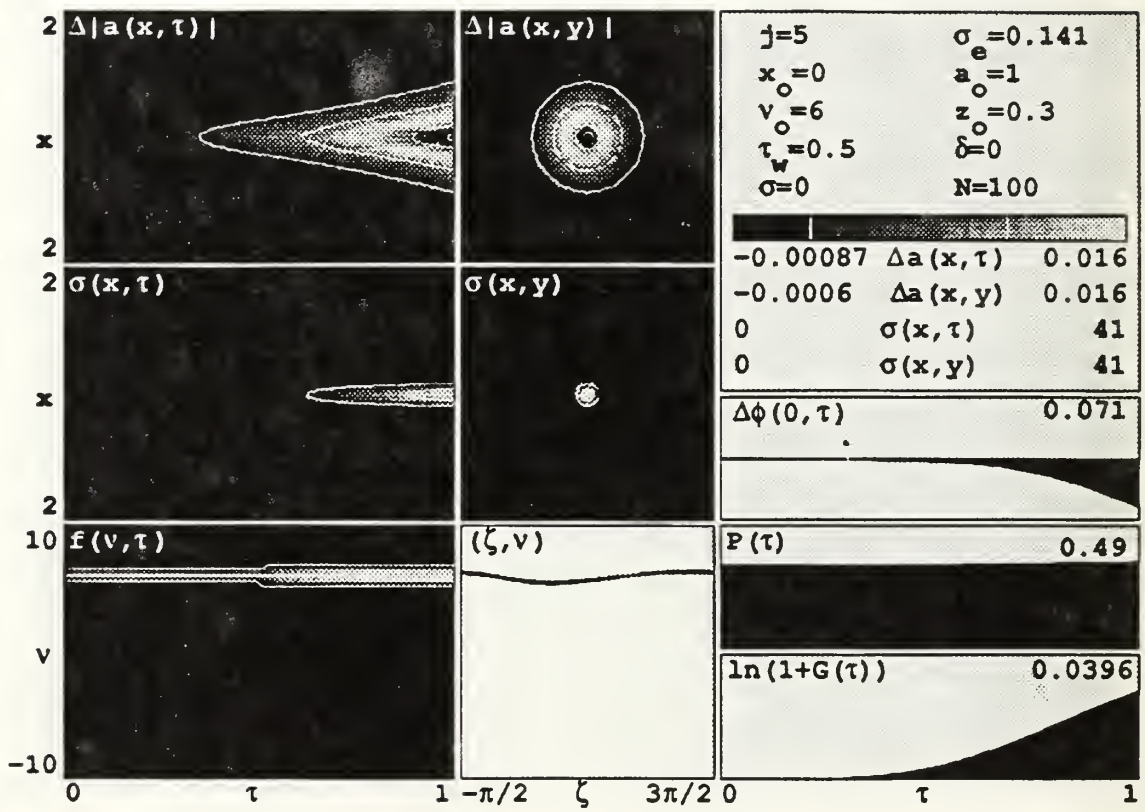

Figure 6-5: The excited optical field of a low gain FEL with a small electron beam. A hole has developed in the excited optical field.

The explanation of this hole involves the relative phase between the new light emitted along the undulator. In the development of equation 5-3 in Chapter V, the phase of the Gaussian optical mode was expanded to

$$\phi_G(\tau) \approx -\frac{(\tau-\tau_w)}{z_0^2} + \frac{r^2(\tau-\tau_w)^2}{z_0^2} + \ldots \quad . \qquad 6\text{-}1$$

At the undulator axis ($r \approx 0$) the relative phase between the optical mode at any two points separated by $\Delta\tau$ is

$$\Delta\phi_G \approx -\frac{\Delta\tau}{z_0} \quad . \qquad 6\text{-}2$$

The effective mode waist for the excited field is roughly equal to the electron beam size so that, $z_0 \approx \sigma_e^2$. The phase shift in equation is then $\Delta\phi_G \approx \Delta\tau/\sigma_e^2$. When $\Delta\phi_G = \pi$ the excited optical field is eliminated by destructive interference when $\sigma_e \approx \sqrt{(\Delta\tau/\pi)}$. The first light emitted near $\tau \approx 0.6$ destructively interferes with light emitted at the end of the undulator, $\tau = 1$, when $\sigma_e \approx 0.36$.

Figures 6-6 and 6-7 show two additional examples of this destructive interference phenomenon. These figures, unlike Figures 6-1 through 6-7, are plotted with a greyscale which runs from white to black with increasing magnitude and no contours. This allows a better display of the thin, excited optical mode and electron beam. Also, the transverse window width of the displays is 8 instead of 4 because of the increased diffraction by the narrow electron beam.

In Figure 6-6 the simulation is run with $j = 10$ and $\sigma_e = 0.1$, so that the product of $j\,\sigma_e^2$ remains 0.1 for low gain. The destructive interference is seen along the undulator axis extending along the final third of the undulator.

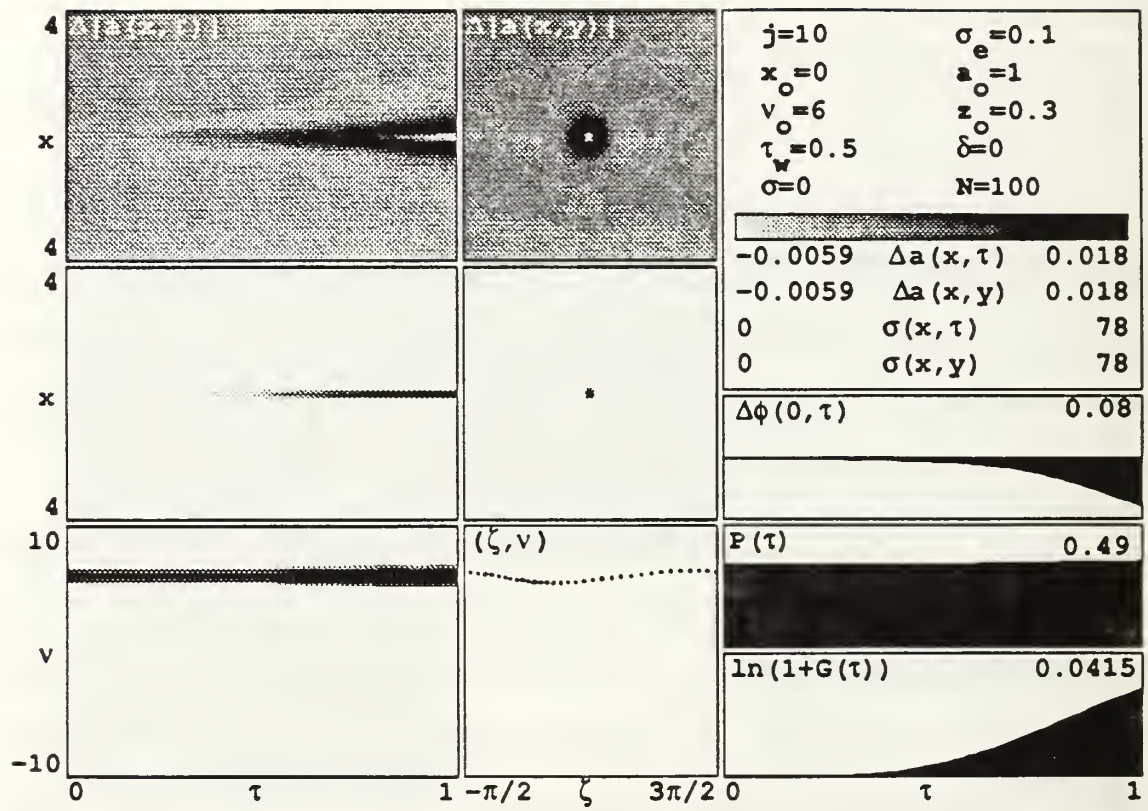

Figure 6-6: The excited optical field of a low gain FEL with electron beam size σ_e = .1. The area of destructive interference extends over the final third of the undulator.

Figure 6-7 is the same type of output with $j = 40$ and $\sigma_\theta = 0.05$ so that $j\sigma_\theta^2 = 0.1$ again. Here, the area of total destructive interference extends through the entire second half of the undulator. This shows that the simple analysis above is correct.

The above explanation of the destructive interference is simple but valid. Actually, light is continuously emitted along the undulator and the amplitude of the light emitted is proportional to the gain. A complex integral is required to fully explain the phase relation that leads to destructive interference. However, the simple argument shows that as the electron beam radius decreases the area of destructive interference within the excited optical mode will extend toward the front of the undulator.

E. THE EFFECT OF GAIN ON MODE DISTORTION

In order to examine the effect of gain on optical mode distortion, the electron beam size is held constant while the dimensionless current density is increased. Figures 6-8 and 6-9 are two examples.

Figure 6-8 shows a low gain system with $j = 0.1$ and $\sigma_\theta = 0.5$. The final gain is only ≈ 0.5% and the power remains roughly constant over the length of the undulator. The maximum amplitude difference between the input optical mode and the total optical mode is small ($\Delta|a|_{max} \approx 0.002$), as expected from low gain. With the moderate electron beam size, the excited optical amplitude difference diffracts with a Rayleigh length $z_\theta \approx 1/\sqrt{2}$. This is roughly twice the input optical Rayleigh length $z_0 = 0.3$ so the excited mode spreads at roughly half the rate of the input mode. The phase difference along the axis is small.

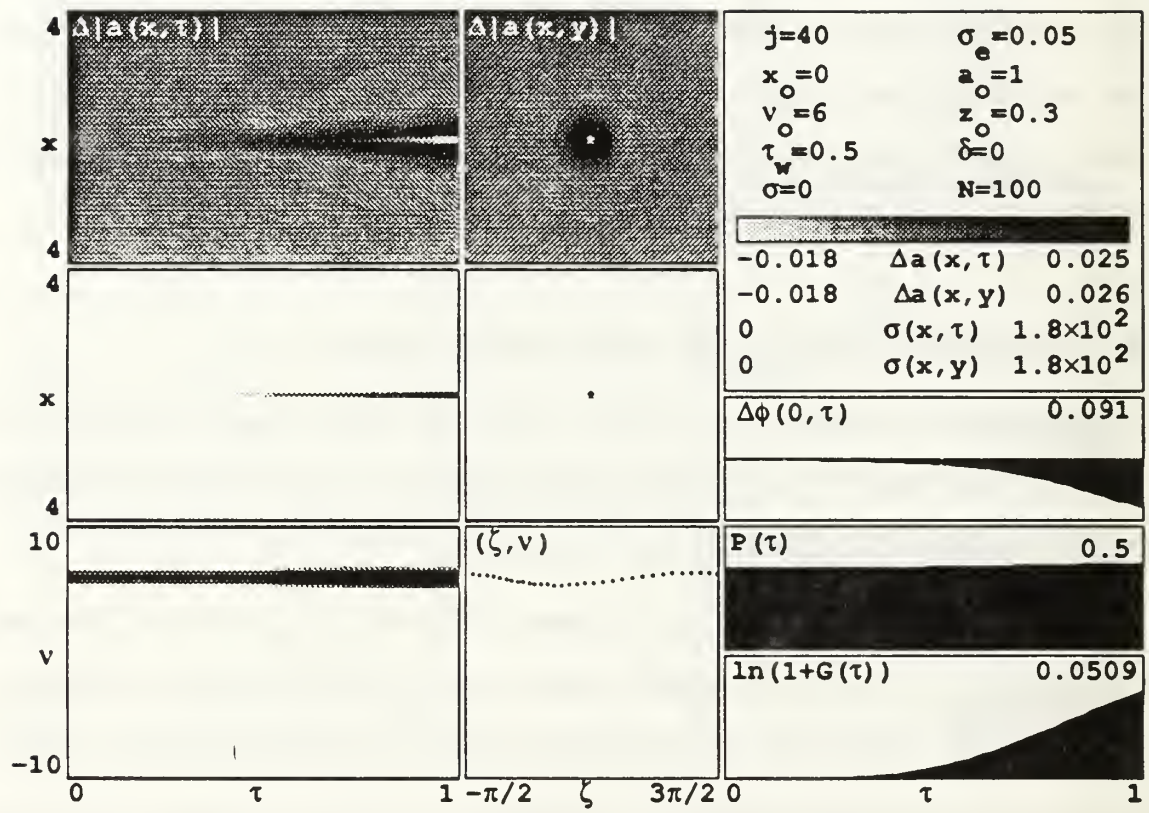

Figure 6-7: The excited optical field of a low gain FEL with electron beam size σ_θ = .05. The area of destructive interference extends over the entire second half of the undulator.

Figure 6-9 shows the excited mode of a high gain system. Here the electron beam is the same as in Figure 6-8, but the dimensionless current density is three orders of magnitude larger. At the lower-right of Figure 6-9, the final gain is 18.5% and the power has grown significantly. The profile of the excited mode at the upper left again shows diffraction at roughly half the rate of the input mode.

It is interesting to note that the plots of the excited optical modes in Figures 6-8 and 6-9 apper to be almost identical. The contours of Figure 6-8 appear somewhat longer, but the shapes are similar. There is a difference in the optical phase evolution in the two plots. In Figure 6-8, the phase difference is very small ($\Delta\phi = 0.0046$), so there is nearly maximum constructive interference along the undulator axis. In Figure 6-9 the phase difference is still small ($\Delta\phi = 0.5$), but more significant. The interference between the input optical mode and the excited optical mode along the undulator axis is not maximized.

F. DISCUSSION

The three-dimensional simulation displaying the excited optical field amplitude and phase provides a useful tool for examining optical mode distortion. The effective Rayleigh length of the excited optical field is $\approx \sigma_e^2$ and the diffraction of the excited optical field is dependent upon the beam radius. The destructive interference caused by the phase difference, $\Delta\phi \approx \Delta\tau/\sigma_e^2 \approx \pi$, when $\Delta\tau \approx 1/3$ occurs when $\sigma_e \approx 0.3$ and leads to the development of a hole within the excited optical mode.

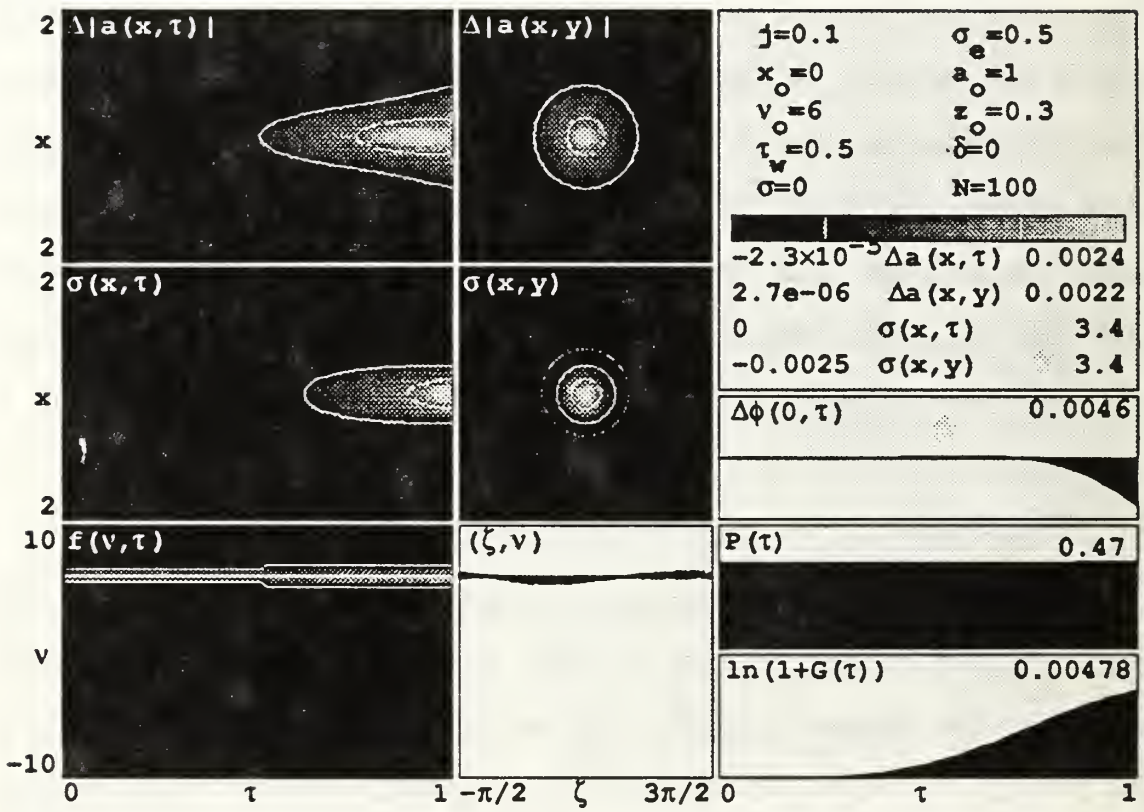

Figure 6-8: The excited optical field of a low gain FEL.

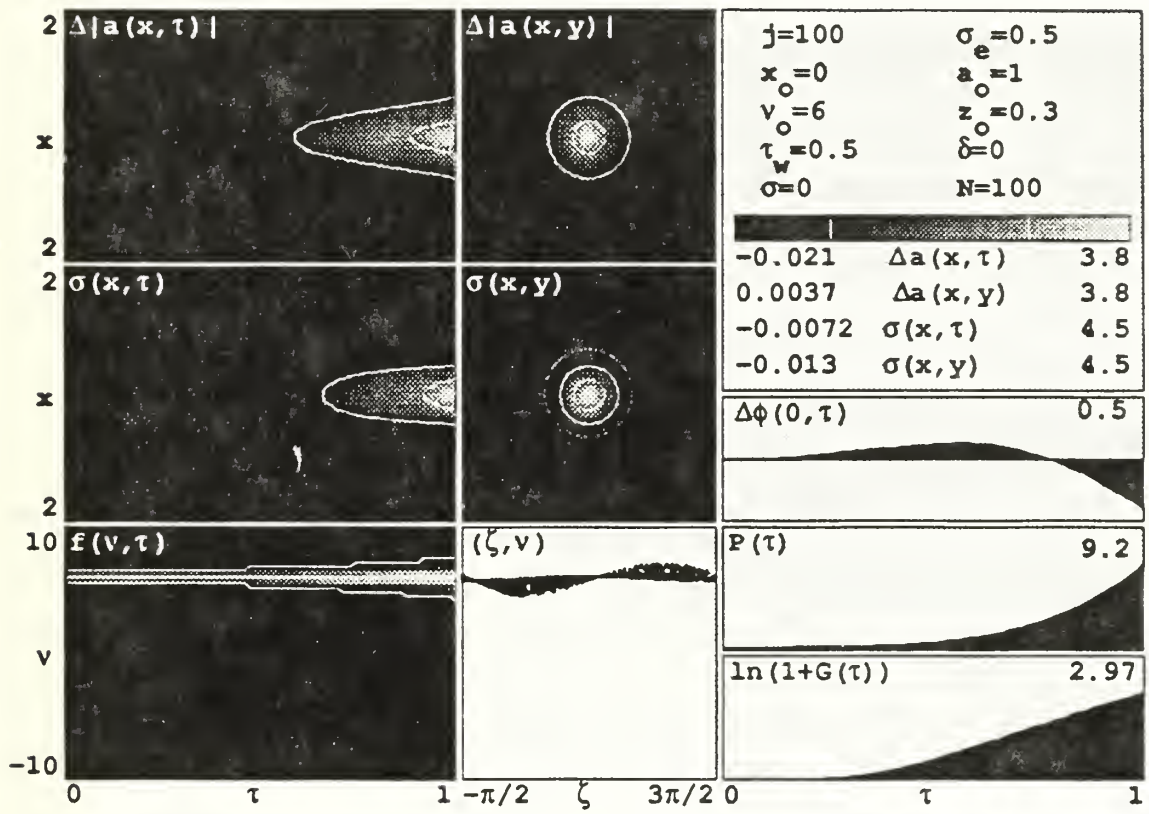

Figure 6-9: The excited optical field of a high gain FEL.

With constant electron beam size, the shape of the excited optical field appears to be relatively independent of the FEL gain. For both a low gain system ($j = 0.1$) and a high gain system ($j = 100$) the shape of the excited optical mode is roughly constant.

Further use of this tool to study the excited optical mode may lead to additional, more significant, insights into optical mode distortion.

VII. CONCLUSIONS

The development of FELs as a source of coherent radiation is continuing as several theoretical and technological issues are met and resolved. The military applications of the FEL, whether on the ground, in space, or aboard a ship has several significant advantages over conventional kinetic systems and other high-energy laser systems. The rapid response, wavelength tuneability, and "infinite" magazine make the FEL a highly desirable system for shipboard use. The all-electric operation of the FEL is especially attractive when coupled with the design of the Navy's all-electric ship. With these important attributes, research should continue toward the development of high power FELs with the goal of shipboard application.

The proposed CEBAF UV FEL represents a significant demonstration of the technologies required for a high power FEL. The superconducting accelerator, high-average power, and short wavelength of the CEBAF UV FEL will reach the highest levels of performance ever demonstrated. Simulations of the proposed experiment presented in Chapter IV helped in the FEL design selection. The designs presented appear feasible and should result in successful accomplishment of the design goals.

In short-wavelength FELs, such as the CEBAF UV FEL, the optical mode is small and can be roughly the same size as the electron beam. The shift in the resonant phase velocity resulting from the injection of electrons away from the undulator axis is predicted in Chapter V. In some instances this shift can be significant. There is also an inevitable reduction in gain resulting from the

off-axis electrons interacting with the weaker optical fields. The gain of such a system can be predicted with the aid of the universal curve also presented in Chapter V.

Optical mode distortion is a key topic in the understanding of the FEL. A new tool presented in Chapter VI helps examine and understand this phenomenon. The modified three-dimensional FEL simulation displays the excited optical mode in the undulator. The size of the electron beam has a significant effect on the characteristics of the excited optical mode. For very small electron beams the phase difference between new light emitted near the axis along the undulator can result in total destructive interference within the excited optical mode. This interference can cause a "dimple" to occur at the center of the total optical field. This dimple and other effects in the excited optical mode could be researched further with the aid of the modified simulation.

LIST OF REFERENCES

[1] J.M.J. Madey, "Stimulated Emission of Radiation in Periodically Deflected Electron Beams," *Journal of Applied Physics*, v.42, 1906, 1971.

[2] R. Holzer, "Navy's antiair warfare plan targets regional threats," *Navy Times*, November 18, 1991.

[3] N. Bloembergen, and others, "Report to the American Physical Society of the study group on science and technology of directed energy weapons," *Reviews of Modern Physics*, v.59 No.3 Part II, July 1987.

[4] Lockheed Missile and Space Company, Inc., Astronautics Division, Lockheed Document Number LMSC-L075685, *Space Based Laser Phase III Final Review*, October 22-23, 1987.

[5] TRW Inc. Electronics and Defense Sector, *Ship Missile Defense Free Electron Laser*, S. Fornaca and H. Thompson, Jr., December 1, 1989,

[6] J. Bell, *Thunderball*, W.J.Schafer Associates, 1901 North Fort Myer Drive, Arlington, VA 22209.

[7] John P. Casey, *AC Electrical Drive Machinery Design*, GE Naval & Drive Turbine Systems, Presented at the 1990 Chesapeake Marine Engineering Symposium, The Society of Naval Architects and Marine Engineers, Arlington, VA, March 14, 1990.

[8] K-J Kim and A. Sessler, "Free Electron Lasers: Present Status and Future Prospects," *Science*, v.250, October 5, 1990.

[9] Air Force Cambridge Research Laboratories, Environmental Research Paper 400, *Atmospheric Attenuation of HF and DF Laser Radiation*, R. A. McClatchey and J.E.A. Selby, May 23, 1972.

[10] F.G. Gebhardt, "High Power Laser Propagation," *Applied Optics*, v.15 No.6, June 1976.

[11] Continuous Electron Beam Accelerator Facility, *High-Power UV and IR Free Electron Lasers Using the CEBAF Superconducting Accelerator*, Vol.1, Newport News, Va, October, 1991.

[12] A.L. Throop, and others, "Experimental Characteristics of a High-Gain Free Electron Laser Amplifier Operating at 8 mm and 2 mm Wavelengths," prepared for AIAA 19th Fluid Dynamics Plasma Division and Laser Conf. Honalulu, Hawaii, June 8-10, 1987.

[13] R.W. Warren, and others, "Recent Results from the Los Alamos Free Electron Laser," *Nuclear Instruments and Methods in Physics Research*, A259, North-Holland, Amsterdam, 1987.

[14] D.W. Feldman, and others, "Energy Recovery in the Los Alamos Free Electron Laser," *Nuclear Instruments and Methods in Physics Research* A259, 26-30 North-Holland, Amsterdam, 1987.

[15] R. Hobbs, *Marine Navigation 1: Piloting*, Naval Institute Press, Maryland, 1974.

[16] J.B. Murphy and C. Pellegrini, "Introduction to the Physics of the FEL," Chapter 2 in *Free Electron Laser Handbook*, W.B Colson, C. Pellegrini and A. Renieri (eds.) North-Holland Physics, Elsevier Science Publishing Co. Inc., The Netherlands 1990.

[17] W.B. Colson, "Classical Free Electron Laser Theory", Chapter 5 in *Free Electron Laser Handbook*, W.B. Colson, C. Pellegrini and A. Renieri (eds.), North-Holland Physics, Elsevier Science Publishing Co. Inc., The Netherlands 1990.

[18] J.D. Jackson, *Classical Electrodynamics*, John Wiley & Sons, New York, 1975.

[19] W.B. Colson and J.L. Richardson, "Multimode Theory of Free Electron Laser Oscillators," *Physics Review Letters*, v.50, 1050, 1983.

[20] C.A. Bice and W.B. Colson, "The CEBAF Ultraviolet FEL Experiment," *Nuclear Instruments and Methods in Physics Research*, AXXX, xxxx-xxxx, 1992. accepted for publication December, 1991.

[21] W. B. Colson and P. Elleaume, "Electron Dynamics in Free Electron Laser Resonator Modes," *Applied Physics B*, v.29, 101-109, 1982.

[22] J.B. Kortright, "Extreme Ultraviolet and Soft X-Ray Optics for Free Electron Lasers," Chapter 13 in *Free Electron Laser Handbook*, W.B. Colson, C. Pellegrini and A. Renieri (eds.), North-Holland Physics, Elsevier Science Publishing Co. Inc., The Netherlands 1990.

[23] A. Amir and Y. Greenzweig, "Three-Dimensional Free Electron Laser Gain and Evolution of Optical Modes," *Nuclear Instruments and Methods in Physics Research*, A250, 404-412, North Holland, Amsterdam, 1986.

[24] C-M Tang and P. Sprangel, "The Three-Dimensional Non-Linear Theory of the Free Electron Laser Amplifier," *Physics of Quantum Electronics*, v.9,*Free-Electron Generators of Coherent Radiation*, Addison-Wesley, 1984.

INITIAL DISTRIBUTION LIST

1.	Defense Technical Information Center Cameron Station Alexandria, Virginia 22304-6145	2
2.	Library, Code 52 Naval Postgraduate School Monterey, California 93943-5002	2
3.	Professor William B. Colson, Code PH/Cw Department of Physics Naval Postgraduate School Monterey, California 93943-5000	7
4.	Professor John R. Neighbours, Code PH/Nb Department of Physics Naval Postgraduate School Monterey, California 93943-5000	1
5.	Professor K. E. Woehler Code PH/Wh Chairman, Department of Physics Naval Postgraduate School Monterey, California 93943-5000	1
6.	Capt. R.M. Cassidy Aegis Program Office James Polk Bldg. 2521 Jefferson Davis Dr. NC 2 10th Floor Arlington, Virginia 22202	1
7.	Dr. David Merrit SPAWAR 23 Space and Naval Warfare Systems Command RM 309, 5 Crystal Park 2451 Crystal Drive Arlington, Virginia 22202	1

Thesis
B51127 Bice
c.1 Theory for the CEBAF
and shipboard FELs.

Thesis
B51127 Bice
c.1 Theory for the CEBAF
and shipboard FELs.

DUDLEY KNOX LIBRARY
3 2768 00031951 1